communications biology

A Nature Portfolio journal

Article

https://doi.org/10.1038/s42003-025-08174-w

Nanoparticle-mediated targeting of PGC-1α reveals critical metabolic pathways in bladder cancer metastasis

Zhenghua Liu[1,4], Peng Xin[2,4], Weiwei Wu[2,4], Mingyue Jin[3], Yang Du[2], Yuanjun Jiang[2] ✉, Tao Liu[2] ✉ & Hao Zhang[2] ✉

Metastatic bladder cancer is characterized by its aggressive behavior and complex molecular mechanisms that remain largely undefined. This study explores the therapeutic potential of targeting peroxisome proliferator-activated receptor gamma coactivator 1-alpha (PGC-1α) using liposomal nanoparticles to deliver PGC-1α siRNA to bladder cancer cells. We employed comprehensive transcriptomic, proteomic, and metabolomic analyses to investigate the impact of PGC-1α silencing. Our in vitro results demonstrate that targeting PGC-1α significantly impairs mitochondrial function and disrupts energy metabolism, affecting critical pathways such as glycolysis and the citric acid cycle, as well as altering mRNA nuclear export. In vivo experiments in animal models show that nanoparticles loaded with si-PGC-1α effectively reduce lung metastasis, indicating a significant impact on metastatic progression. These findings highlight PGC-1α as a key regulator of metabolic reprogramming in metastatic bladder cancer and suggest that its inhibition could serve as a promising therapeutic strategy. By elucidating the role of PGC-1α in cancer metabolism, this study provides new insights into the molecular underpinnings of bladder cancer metastasis and offers potential avenues for developing targeted therapies aimed at the metabolic vulnerabilities of this malignancy.

In recent years, there has been an increasing incidence of metastatic bladder cancer, a highly aggressive and lethal nature that poses a significant threat to patients worldwide[1–4]. Currently, therapeutic options for metastatic bladder cancer remain limited, highlighting the urgent need for novel treatment strategies and a better understanding of the molecular mechanisms underlying this disease[5–7]. The emerging field of nanotechnology, in particular the use of liposomal nanoparticles for siRNA delivery, has gained significant attention as a potential therapeutic approach for cancer treatment[8,9].

Nanotechnology has made significant progress in cancer treatment, particularly in targeted drug delivery and gene therapy[8,9]. Liposomal nanoparticles, as an important nanocarrier, have become a research hotspot due to their excellent biocompatibility, controllable release properties, and ability to effectively deliver large molecules such as siRNA[10]. These nanoparticles not only address the inefficiencies and side effects of traditional drug delivery methods but also enhance targeting and therapeutic effects through surface modifications[11,12]. For example, ACC/CaIP 6 nanoparticles have been successfully used to deliver siRNA in breast cancer gene therapy, showing potential in inhibiting cancer cell growth[13]. While significant progress has been made in the use of liposomal nanoparticles for siRNA delivery in cancers, the application of these nanoparticles to deliver PGC-1α siRNA in bladder cancer remains underexplored, and the specific role of PGC-1α requires further investigation. Therefore, there is an urgent need to explore how liposomal nanoparticles can target PGC-1α to offer a novel, low side-effect therapeutic strategy for bladder cancer.

PGC-1α, a co-activator that regulates cellular energy metabolism, plays a crucial role in normal cell functions[14,15]. However, abnormal expression of PGC-1α has been linked to tumor development, metabolic reprogramming, and altered energy metabolism in cancer cells[16–18]. PGC-1α is also a key regulator of mitochondrial biogenesis, influencing processes like oxidative phosphorylation, thermogenesis, and fatty acid biosynthesis and degradation[19,20]. Under conditions of cellular bioenergetic stress, PGC-1α supports ATP production, helping cells resist necrosis and apoptosis[21].

[1]Department of Thoracic Surgery, The First Hospital of China Medical University, Shenyang, Liaoning, 110001, P.R. China. [2]Department of Urology, The First Hospital of China Medical University, Shenyang, Liaoning, 110001, P.R. China. [3]Department of Endocrinology, Shenzhen University General Hospital, Shenzhen, Guangdong, 518055, P.R. China. [4]These authors contributed equally: Zhenghua Liu, Peng Xin, Weiwei Wu. ✉e-mail: 13804064945@163.com; cmuliu2016@163.com; Lunar8511@126.com

Additionally, PGC-1α's C-terminal domain, particularly its serine/arginine-rich region, enables binding to RNA and regulating transcription[22–24]. This RNA binding influences mRNA splicing and nuclear export through interactions with transcription and splicing factors[25–27]. Studies using eCLIP technology have demonstrated that PGC-1α specifically interacts with certain mRNA transcripts, suggesting its potential involvement in RNA metabolism[28]. However, the exact role of PGC-1α in tumor metastasis remains unclear[29].

Given its involvement in metabolic reprogramming and mitochondrial function, targeting PGC-1α could represent a promising strategy for inhibiting metastatic bladder cancer progression and reducing its metastatic potential[30,31]. A promising approach for minimizing systemic side effects is the direct, local delivery of therapeutic siRNA to the target tissue[32]. Intratumoral siRNA delivery has been shown to effectively inhibit tumor growth in mouse models of cervical cancer[33]. Similarly, in bladder cancer treatment, intravesical injection of chemotherapeutic agents has become a preferred method to prevent postoperative tumor recurrence while avoiding systemic side effects, demonstrating the potential benefits of local siRNA delivery[32].

Therefore, this study aims to develop a liposomal nanoparticle-based delivery system for PGC-1α siRNA and comprehensively investigate its effects on bladder cancer cells using transcriptomic, proteomic, and metabolomic technologies. We hypothesize that silencing PGC-1α can significantly alter mitochondrial function and energy metabolism in bladder cancer cells, thereby inhibiting their metastatic potential and providing a novel therapeutic approach. To achieve this, we will utilize transcriptomics, proteomics, and metabolomics analyses to evaluate the effects of PGC-1α silencing on bladder cancer cell metabolism, mitochondrial function, and metastatic potential. Additionally, we have developed a liposomal nanoparticle system for delivering PGC-1α siRNA and assessed its transfection efficiency, cytotoxicity, and impact on gene expression in bladder cancer cells.

Results

Differential regulation of mitochondrial function and upregulation of PGC-1α in metastatic bladder cancer

To screen for genes potentially impacting bladder cancer metastasis for the purpose of delivering siRNA to bladder cancer cells for treatment, we used a GFP-labeled T24 human bladder cancer cell line and injected it into the bladders of nude mice, establishing a mouse model of bladder cancer (Fig. 1A). By performing tissue sectioning and H&E staining, we successfully confirmed the establishment of the model (Fig. 1B). Subsequently, we collected samples of in situ bladder cancer and metastatic bladder cancer tissues. Through flow cytometry sorting, we obtained PBCC and MBCC, then extracted RNA from these cells for transcriptome sequencing (Fig. 1A).

Using a significance level of $P < 0.05$ as the filtering criterion, we identified 937 differentially expressed genes in MBCCs compared to PBCC, of which 443 genes were upregulated, and 494 genes were downregulated (Fig. 1C). Functional enrichment analysis of these differentially expressed genes revealed involvement in various biological processes, including lipid metabolism, mitochondrial gene expression, regulation of mitochondrial structure, regulation of cellular catabolic metabolism, and carbohydrate metabolism (Fig. 1D). This suggests a significant difference in metabolic processes between MBCCs and in situ bladder cancer cells.

Furthermore, further analysis revealed significant upregulation of genes related to mitochondrial dynamics (PGC-1α, PGC-1β, NRF1, and ESRRA) and oxidative phosphorylation (COX5B and ATP6V1B1), as well as upregulation of a gene associated with lipid metabolism (glutathione peroxidase 3, GPX3), and downregulation of arachidonate 12-lipoxygenase (ALOX12), FABP5L2, and GPX7 in MBCCs (Fig. 1E).

Interestingly, in MBCCs, the expression level of PGC-1α exceeds that of other known promoters of mitochondrial biogenesis, including ESRRA, NRF1, and PGC-1β (Fig. 1E). Immunostaining analysis of PBCCs and MBCCs for PGC-1α illustrates a significantly higher expression proportion in MBCCs (Fig. 2A). The Western blot results showed that MBCCs express more PGC-1α than PBCCs (Fig. 2B). This suggests that PGC-1α plays a distinct regulatory role in MBCCs, potentially being closely associated with the requirements for tumor growth and metastasis.

To validate the significant increase in PGC-1α in MBCCs and its association with cellular mitochondrial quantity and respiration, we measured the mitochondrial DNA content, ATP production, and OCR in purified MBCCs. The results demonstrate a significantly increased mitochondrial DNA content in MBCCs compared to PBCCs (Fig. 2C), higher levels of intracellular ATP (Fig. 2D), increased basal respiration rate (Fig. 2E), and enhanced mitochondrial OCR (Fig. 2F).

These findings suggest that enhanced oxidative phosphorylation of mitochondria is associated with an increase in the number of mitochondria per cell, while the significant elevation of PGC-1α expression and mitochondrial biogenesis are distinguishing features of MBCCs.

Inhibition of cellular energy metabolism and mitochondrial morphology alterations in bladder cancer cells by liposomal nanoparticles delivering PGC-1α siRNA

In our investigation of mBC, we observed a significant upregulation of PGC-1α expression, which is associated with increased mitochondrial biogenesis and energy metabolism. This suggests the potential importance of PGC-1α in therapy. Therefore, our aim was to construct a liposomal nanoparticle system for delivering PGC-1α siRNA to study its mechanisms of action in bladder cancer, particularly its role in regulating tumor cell energy metabolism and chemotherapy-induced cachexia.

Through a literature review, we identified a sequence of siRNA[34] that effectively reduces PGC-1α protein levels. We constructed liposomal nanoparticles for delivering PGC-1α siRNA using the ethanol injection method followed by dialysis (Fig. S1A). These liposomal nanoparticles had a size of 79.91 ± 0.35 nm (Fig. S1B), and dynamic light scattering confirmed a surface charge of 38 mV (Fig. S1C).

To assess the uptake efficiency of si-PGC-1α LNP in the human bladder cancer cell line T24, we co-cultured T24 cells with si-PGC-1α LNP and analyzed the uptake rate using fluorescence microscopy and flow cytometry. The results demonstrated that the human bladder cancer cells efficiently internalized si-PGC-1α LNP, with an uptake rate of approximately 75.5% (Fig. S1D-E).

In conclusion, we successfully developed an LNP system for efficiently delivering siRNA into bladder cancer cells. These LNPs exhibited high uptake rates and good biocompatibility.

To evaluate the inhibitory effect of si-PGC-1α LNP on PGC-1α protein expression, T24 cells were co-cultured with si-PGC-1α LNP or LNP (Fig. 3A). After culturing, cells were collected, and the impact of si-PGC-1α LNP on PGC-1α protein levels in T24 cells was analyzed. The results showed a significant decrease in PGC-1α protein expression with si-PGC-1α LNP treatment (Fig. 3B, C). Additionally, a series of experiments were conducted to determine if the significant decrease in PGC-1α protein levels induced by si-PGC-1α LNP had any effect on the morphology of mitochondria in T24 cells (Fig. 3A).

We found that compared to the LNP group, the si-PGC-1α LNP group exhibited reduced mitochondrial DNA and ATP content in cells (Fig. 3D, E). TEM analysis revealed a decrease in the number of mitochondria in the si-PGC-1α LNP group, as well as swelling, disorganization, and disruption of internal structure within the mitochondria (Fig. 3F, G). These findings suggest that the significant decrease in PGC-1α protein levels caused by si-PGC-1α LNP leads to inhibition of mitochondria biogenesis.

Moreover, this was further validated through a series of mitochondrial stress tests on cultured cells. These experiments demonstrated that the si-PGC-1α LNP group exhibited a significantly lower basal respiration rate compared to the LNP group (Fig. 3H, "1"). We noticed that after inhibiting electron transport chain complexes I + II, the non-mitochondrial respiration rate increased significantly in the LNP group cells, whereas the increase in the si-PGC-1α LNP group was less pronounced (Fig. 3H, "2").

Measurement of mitochondrial respiration rate also revealed a decreased ATP-coupled respiration rate and increased proton leak in

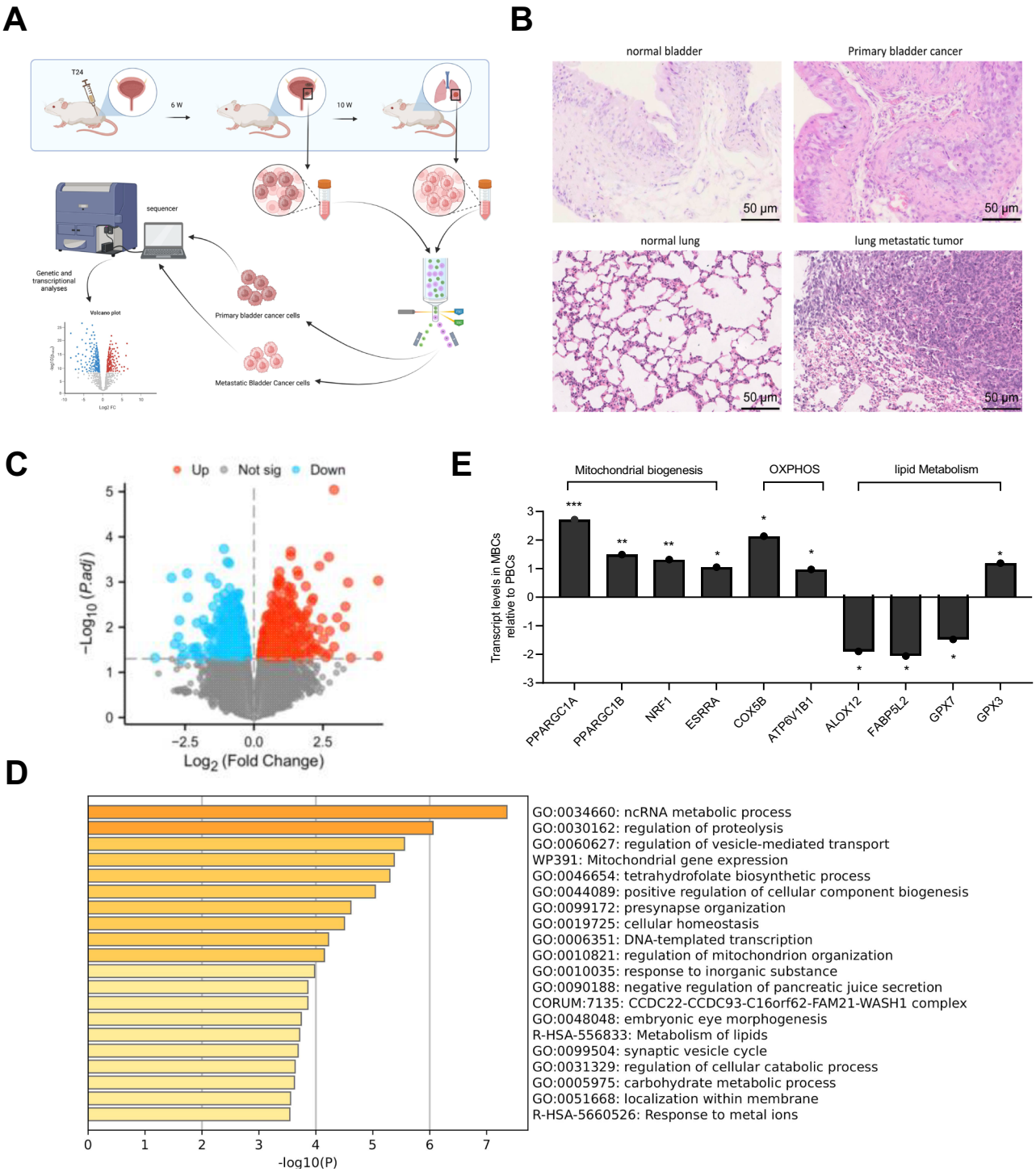

Fig. 1 | Analysis of gene expression differences between PBCCs and MBCCs. **A** GFP + T24 cells were orthotopically injected into the bladder of nude mice, and PBCCs and MBCCs were isolated from three different samples using fluorescence-activated cell sorting (FACS sorting) for RNA-seq and data analysis (created by BioRender); (**B**) H&E staining confirmed the successful construction of the bladder cancer mouse model, with N representing normal tissue and M representing tumor tissue, the bar in the image equals 50 μm (200×); (**C**) The volcano plot demonstrates the differential gene expression between PBCCs and MBCCs, with blue dots indicating downregulated genes, red dots indicating upregulated genes, and gray dots indicating genes with no significant difference; (**D**) Differential gene expression analysis was performed using the online analysis tool Metascape, revealing their biological functions; (**E**) Transcriptome analysis revealed significantly different expression levels of mitochondria morphology-related genes (such as PGC-1α, PGC-1β, NRF1, and ESRRA), oxidative phosphorylation-related genes (such as COX5B and ATP6V1B1), and lipid metabolism-related genes (such as GPX3, ALOX12, FABP5L2, and GPX7) between PBCCs and MBCCs, indicated by ***$P < 0.001$, **$P < 0.01$, and *$P < 0.05$.

si-PGC-1α LNP group cells compared to the LNP group cells (Fig. 3I, B' < B; C' > C). The si-PGC-1α LNP group cells exhibited maximal capacity respiration (Fig. 3H, D' < A) relative to the LNP group cells, potentially compensating for the decreased ATP-coupled respiration due to mitochondrial loss and subsequently reducing basal respiration rate.

The si-PGC-1α LNP cells exhibited lower mitochondrial respiration rates compared to the LNP group cells, even when ETC complex I or

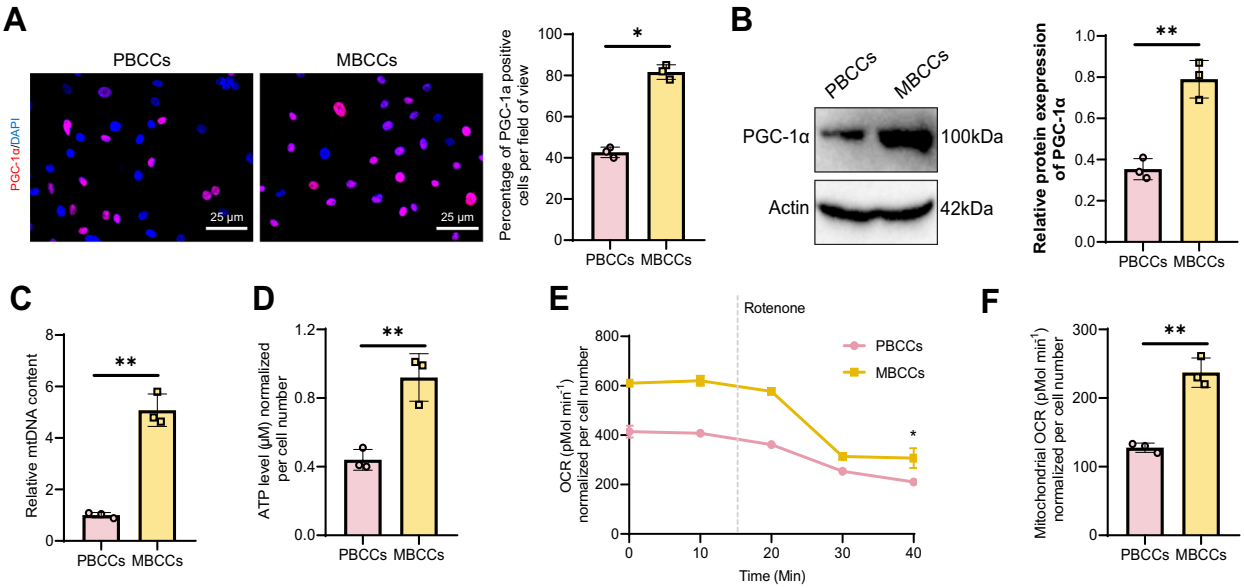

Fig. 2 | Impact of high expression of PGC-1α in MBCCs on OCR associated with mitochondria generation. A Immunostaining for PGC-1α was performed in PBCCs and MBCCs. In the image, PGC-1α is labeled in red, and the nuclei are labeled in blue. The percentage of PGC-1α positive cells was quantitatively analyzed. Scale bar = 25 μm (400×); (**B**) Western blot analysis of PGC-1α protein expression in PBCCs and MBCCs; (**C**) The content of mitochondrial DNA (mtDNA) was measured in PBCCs and MBCCs; (**D**) The intracellular ATP levels were measured in PBCCs and MBCCs; (**E**) OCR before and after Rotenone treatment was compared between PBCCs and MBCCs; (**F**) OCR of mitochondria was compared between PBCCs and MBCCs. All data are presented in the form of mean ± standard deviation. Significance levels are indicated by asterisks, $^{*}P < 0.05$, $^{**}P < 0.01$. This experiment was performed using three samples from three nude mice.

complex I + II were inhibited (Fig. 3J). Compensation through complex II activity was not observed when mitochondrial respiration was impaired due to PGC-1α inhibition in live cells. However, OCR measurements in permeabilized cells suggested differential regulation of complex II-associated OCR activity in the si-PGC-1α LNP group cells (increased OCR after succinate injection) relative to the LNP group cells (Fig. 3K).

In our study, we co-cultured T24 cell lines with LNP and si-PGC-1α LNP to investigate the impact of si-PGC-1α LNP on cell metabolism. We harvested intracellular metabolites within 8 h of culturing and successfully identified the metabolites in both cell groups using LC-MS technology (Fig. 4A). Multivariate statistical analysis revealed significant differences in metabolites between the LNP and si-PGC-1α LNP treatment groups compared to the control group (Fig. 4B–E). Further analysis revealed that, compared to LNP-treated T24 cells, a total of 79 metabolites showed changes in abundance in si-PGC-1α LNP-treated T24 cells, with all P-values less than 0.05 (Fig. 4F). Among these, 42 metabolites were upregulated, with key metabolites in the glycolysis pathway, such as phosphoenolpyruvate (PEP), 3-phosphoglycerate, 2-phosphoglycerate, and the pentose phosphate pathway metabolite D-glyceraldehyde 3-P, showing the most significant upregulation (Log2FC > 3, $P < 0.05$).

Additionally, 37 metabolites were downregulated in si-PGC-1α LNP-treated T24 cells, with key metabolites in purine nucleotide synthesis (AICA ribonucleotide), the tricarboxylic acid (TCA) cycle (oxaloacetic acid), and sphingolipid metabolism (lactosyl-N-nervonoyl-sphingosine (d18:1/24:1)*) being the most significantly downregulated (Log2FC < -3, $P < 0.05$). These results suggest a marked impact of si-PGC-1α LNP treatment on cellular metabolism. We also observed significant changes in metabolites involved in important biological processes, including glycolysis, the TCA cycle, the pentose phosphate pathway, and amino acid metabolism (Fig. 4G–J).

Phosphoenolpyruvate (PEP) plays a critical role in lipid metabolism, particularly in fatty acid synthesis. Additionally, 3-phosphoglycerate plays a role not only in glycolysis but also in lipid metabolism. In lipid synthesis, fatty acids initially react with glycerol-3-phosphate to produce 1-acylglycerol-3-phosphate (LPA) in a reaction catalyzed by glycerol-3-phosphate acyltransferase (GPAT). LPA then reacts with another acyl-CoA to form phosphatidic acid (PA), which is ultimately converted to triacylglycerol (TAG) through a reaction catalyzed by diacylglycerol O-acyltransferase (DGAT). This series of reactions indicates that 3-phosphoglycerate plays a vital role in lipid synthesis metabolism, suggesting a potential impact on lipid metabolism as well.

These findings suggest that si-PGC-1α LNP leads to mitochondrial biogenesis and functional decline in T24 cell lines by suppressing the expression of PGC-1α. This is evidenced by abnormal mitochondrial morphology, reduced ATP production, and changes in metabolic pathways. Moreover, changes in mitochondrial respiration may reflect adaptive responses to cellular energy deficiency, including decreased basal respiration rate and increased proton leak, to maintain the energy balance required for cell survival.

PGC-1α mediated mitochondrial biology and energy metabolism associated with the invasive ability of MBCCs

In our study, we investigated the potential correlation between PGC-1α mediated mitochondrial biology and energy metabolism with the invasive ability of MBCCs. To achieve this, we treated T24 cells with LNP, si-PGC-1α LNP, and LNP+Rotenone and measured their invasive, migratory, and contraction abilities. Our findings revealed a significant decrease in the invasive ability, migration, and cellular contraction of T24 cells treated with si-PGC-1α LNP and LNP+Rotenone compared to the control group that received only LNP treatment (Fig. S2A-C). These results suggest that si-PGC-1α LNP and LNP+Rotenone treatments effectively reduce the invasive and migratory characteristics of cancer cells, indicating that PGC-1α mediated mitochondrial biology and energy metabolism may play a crucial role in maintaining the invasive nature of cancer cells.

Significant Alterations in Mitochondrial Morphology and Function Resulting from si-PGC-1α LNP Treatment in T24 Cell Line

In order to evaluate the molecular mechanism underlying the effect of si-PGC-1α LNP treatment on mitochondrial morphology in the T24 cell line, protein composition analysis was conducted on cell samples from the LNP_T24 group and the si-PGC-1α LNP_T24 group (three samples each). Through this study, we discovered differential protein expression induced by si-PGC-1α LNP treatment. We identified 1745 protein molecules, out of

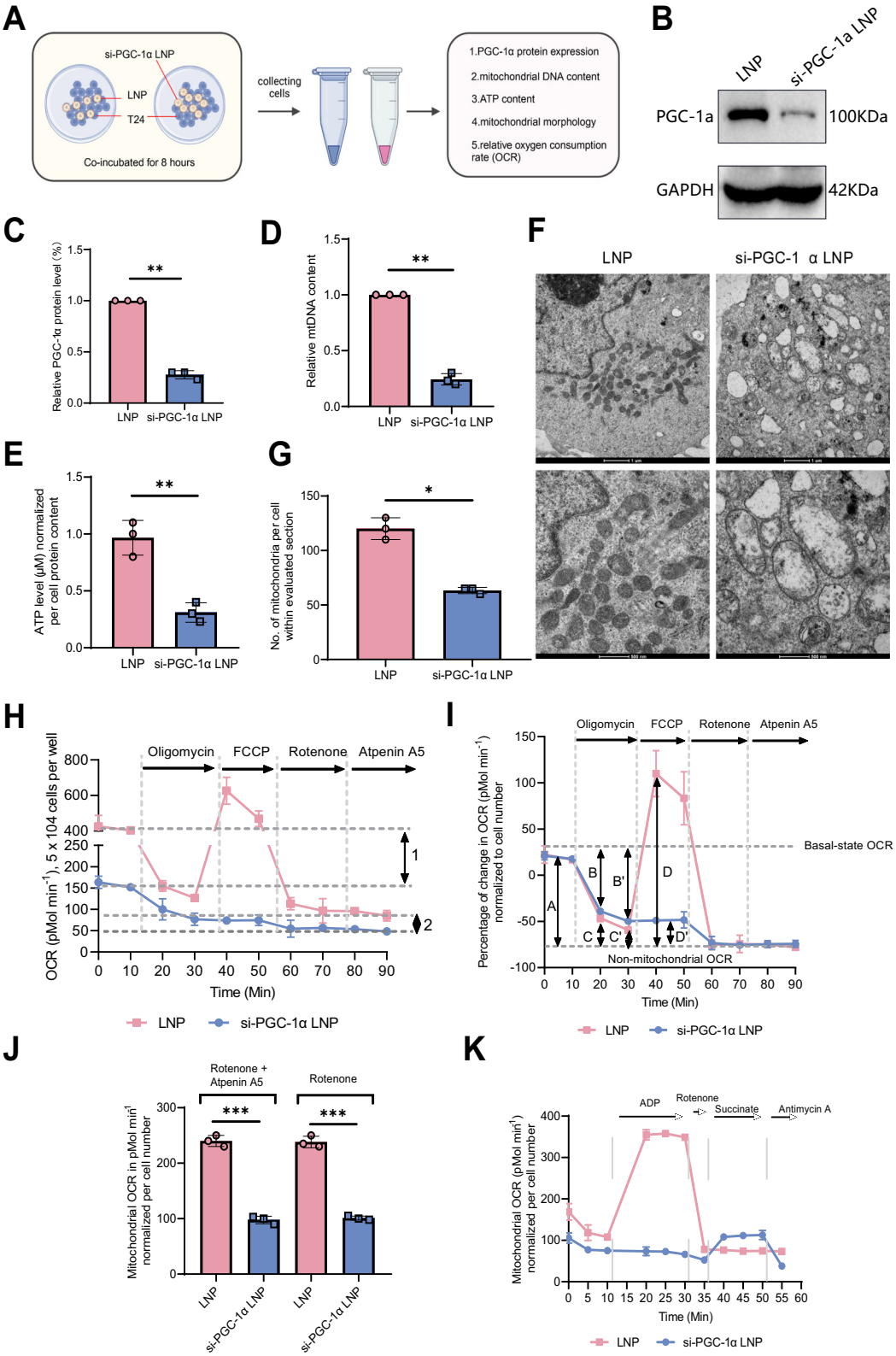

which 200 proteins exhibited significant differential expression, with 159 up-regulated and 41 down-regulated (Fig. 5A).

Based on the functional enrichment analysis of the differentially expressed proteins, we observed significant enrichment changes in several key biological processes and cellular structural components in the si-PGC-1α LNP-treated T24 cell line. This suggests that the intervention of si-PGC-1α may have important implications for cellular metabolism and structure. Specifically (Fig. 5B), the differentially expressed proteins were primarily enriched in metabolic pathways, including the ATP metabolism process, cellular respiration, and the citric acid cycle, indicating a strong impact on cellular energy metabolism. Of particular note, these metabolic pathways are closely associated

Fig. 3 | Impact of si-PGC-1α LNP on the mitochondrial respiration level in T24 cells. A The flowchart presents the procedure for both cell groups (created by BioRender); (**B**, **C**) The influence of LNP or si-PGC-1α LNP on protein expression in the T24 cell line was assessed by Western blot; (**D**) The mtDNA content was determined in T24 cells treated with LNP and si-PGC-1α LNP; (**E**) The ATP content was measured in T24 cells treated with LNP and si-PGC-1α LNP; (**F**, **G**) Scanning electron microscopy was used to observe the morphology and quantity of mitochondria in these two cell groups, with the bar equaling 1 μm (6500×) in the upper image and 500 nm in the lower image (15000×); (**H**) Changes in relative OCR over time, normalized to cell count, were recorded in LNP T24 cells and si-PGC-1α LNP T24 cells, where "1" represents the difference in baseline OCR and "2" represents the difference in non-mitochondrial OCR; (**I**) The percentage change of OCR normalized to cell count, "A" represents the initial OCR, "B" and "B‴ represent the percentage of OCR used for ATP synthesis in LNP T24 cells and si-PGC-1α LNP T24 cells, "C" and "C‴ represent the percentage of OCR associated with proton leak in LNP T24 cells and si-PGC-1α LNP T24 cells, and "D" and "D‴ represent the percentage of OCR of the maximum mitochondrial respiration capacity in LNP T24 cells and si-PGC-1α LNP T24 cells; (**J**) Analysis of changes in mitochondrial OCR in LNP T24 cells and si-PGC-1α LNP T24 cells, including the presence or absence of Atpenin A5 treatment before and after Rotenone treatment, and the results of one-way ANOVA analysis were calculated; (**K**) OCR measurements were recorded in permeabilized LNP T24 cells and si-PGC-1α LNP T24 cells; All data are presented in the form of mean ± standard deviation, * denote significance levels,*$P < 0.05$, **$P < 0.01$, ***$P < 0.001$.

with mitochondrial function, which acts as the cellular energy production center.

Furthermore, changes in molecular functions related to cellular structure and function, such as cell-substrate interactions, cytoplasmic ribosomes, actin cytoskeleton, and components of the ribosomes, were also observed. These enrichment results strongly suggest significant regulation of cellular structures and protein synthesis, particularly in the biological processes associated with mitochondria.

In summary, these findings of functional enrichment analysis not only highlight the significant impact of si-PGC-1α LNP treatment on cellular metabolism and structure but also underscore the high relevance of PGC-1α to mitochondria-related biological processes. The subcellular localization of differentially expressed proteins further confirmed this; specifically, among all the differentially expressed proteins, 37 were localized on mitochondria. Out of these proteins, 10 were part of the mitochondrial protein complex, 7 were located on the outer mitochondrial membrane, and 13 were located on the inner mitochondrial membrane, totaling 19 proteins localized on the mitochondrial membrane (Fig. 5C).

Through PPI network analysis of 37 mitochondria-localized proteins, we identified TFAM, COX10, and COX5A as key players in this network (Fig. 5D). TFAM is primarily involved in maintaining and coordinating the replication and transcription of mitochondria DNA, thereby contributing to the maintenance of mitochondrial function. COX10 participates in the assembly of cytochrome c oxidase, ensuring the normal function of the mitochondrial respiratory chain and supporting cellular energy generation. COX5A, as a subunit of cytochrome c oxidase, facilitates electron transfer in the electron transport chain, thereby promoting cellular energy production.

After si-PGC-1α LNP treatment, we observed a significant downregulation in the expression levels of TFAM, COX10, and COX5A in the cells (Fig. 5E). Of note, the protein levels of NRF1, an upstream regulator of TFAM and one of the traditional targets of PGC-1α, also showed a significant decrease. NRF1 is typically responsible for activating the expression of TFAM, thereby increasing its concentration in the mitochondria (Fig. 5E). This regulatory mechanism is crucial for maintaining normal replication and transcription of mitochondria DNA. Further correlation analysis revealed significant positive relationships among NRF1, TFAM, COX10, and COX5A (Fig. 5F).

Taken together, our findings demonstrate that si-PGC-1α LNP treatment in T24 cells leads to differential expression of key proteins, particularly those involved in mitochondrial morphology and function. The significant downregulation of TFAM, COX10, and COX5A, among other mitochondria-related proteins, highlights the critical role of PGC-1α in maintaining mitochondrial function. Additionally, the notable inhibition of NRF1, an upstream regulator of TFAM, may contribute to abnormalities in mitochondrial DNA replication and transcription.

The role of PGC-1α silencing in the nuclear-cytoplasmic transport process and PGC-1α interaction with NXF1 in mRNA export

Through proteomics analysis, we observed that in T24 cells, si-PGC-1α LNP-mediated PGC-1α silencing significantly reduced the protein levels of NRF1, TFAM, COX10, and COX5A, which are essential for maintaining mitochondrial morphology. Western blot analysis further confirmed the decreased levels of these proteins (Fig. 6A).

It is worth noting that although PGC-1α silencing did not alter the overall levels of NRF1, TFAM, COX10, and COX5A mRNA (Fig. 6B), separation and analysis of mRNA content within the nucleus and cytoplasm revealed that si-PGC-1α LNP treatment significantly increased the mRNA content of these genes in the nucleus (Fig. 6C) while decreasing their content in the cytoplasm (Fig. 6D). This suggests that si-PGC-1α LNP-mediated PGC-1α silencing may lead to mRNA accumulation in the nucleus, thereby hindering its normal transport to the cytoplasm.

Furthermore, Cy3-labeled oligo(dT) FISH experiments further confirmed this observation (Fig. 6E). In cells treated with LNP, Poly-A + RNA was uniformly distributed between the nucleus and cytoplasm, indicating unaffected nuclear-cytoplasmic transport of mRNA. In contrast, in cells treated with si-PGC-1α LNP, Poly-A + RNA mainly accumulated in the nucleus, with significantly reduced signals in the cytoplasm, consistent with the results of mRNA nuclear accumulation observed through PCR experiments. This further supports the regulatory role of PGC-1α in mRNA transport.

To assess the intrinsic correlation of these findings, we conducted RIP experiments using UV-crosslinked and formaldehyde-treated RNA to analyze the interaction between PGC-1α and target gene mRNA. Our experimental results indicate that PGC-1α can bind to these mRNAs, but their enrichment was significantly reduced following si-PGC-1α LNP treatment (Fig. 6F).

Based on our research findings, we propose that PGC-1α may mediate the transport of mRNA from the nucleus to the cytoplasm by interacting with NXF1 within the cell. To test this hypothesis, we conducted PLA experiments. The results (Fig. 6G) showed that in cells treated with LNP, PLA signals mainly accumulated in the nucleus, demonstrating a distinct punctate distribution. However, in cells treated with si-PGC-1α LNP, these signals were significantly reduced.

In addition, we co-transfected FLAG empty vector, FLAG-PGC-1α, and Myc-NXF1 in the T24 cell line, as well as Myc empty vector, FLAG-NXF1, and Myc-PGC-1α, and conducted co-immunoprecipitation (CO-IP) experiments. The results showed an interaction between these two proteins. Overall, these findings strongly suggest that the interaction between PGC-1α and NXF1 plays an important role in the nuclear export of mRNA, and inhibiting PGC-1α weakens the functional interaction of this relationship (Fig. 6H).

The silencing of PGC-1α by si-PGC-1α LNP in T24 cells was found to inhibit nuclear-cytoplasmic transport of mRNA, resulting in its accumulation in the nucleus. Additionally, PGC-1α interacts with NXF1 and plays a pivotal role in mRNA export from the nucleus. These findings reveal a novel function of PGC-1α in cellular RNA metabolism and have important implications for understanding the regulation of nuclear export.

Local delivery, distribution, and anti-metastatic effects of si-PGC-1α LNP in metastatic bladder cancer

To evaluate the uniform distribution of siRNA in a mouse bladder cancer model, we injected si-PGC-1α LNP into subcutaneous xenografts. The distribution of si-PGC-1α was assessed using in vivo imaging techniques.

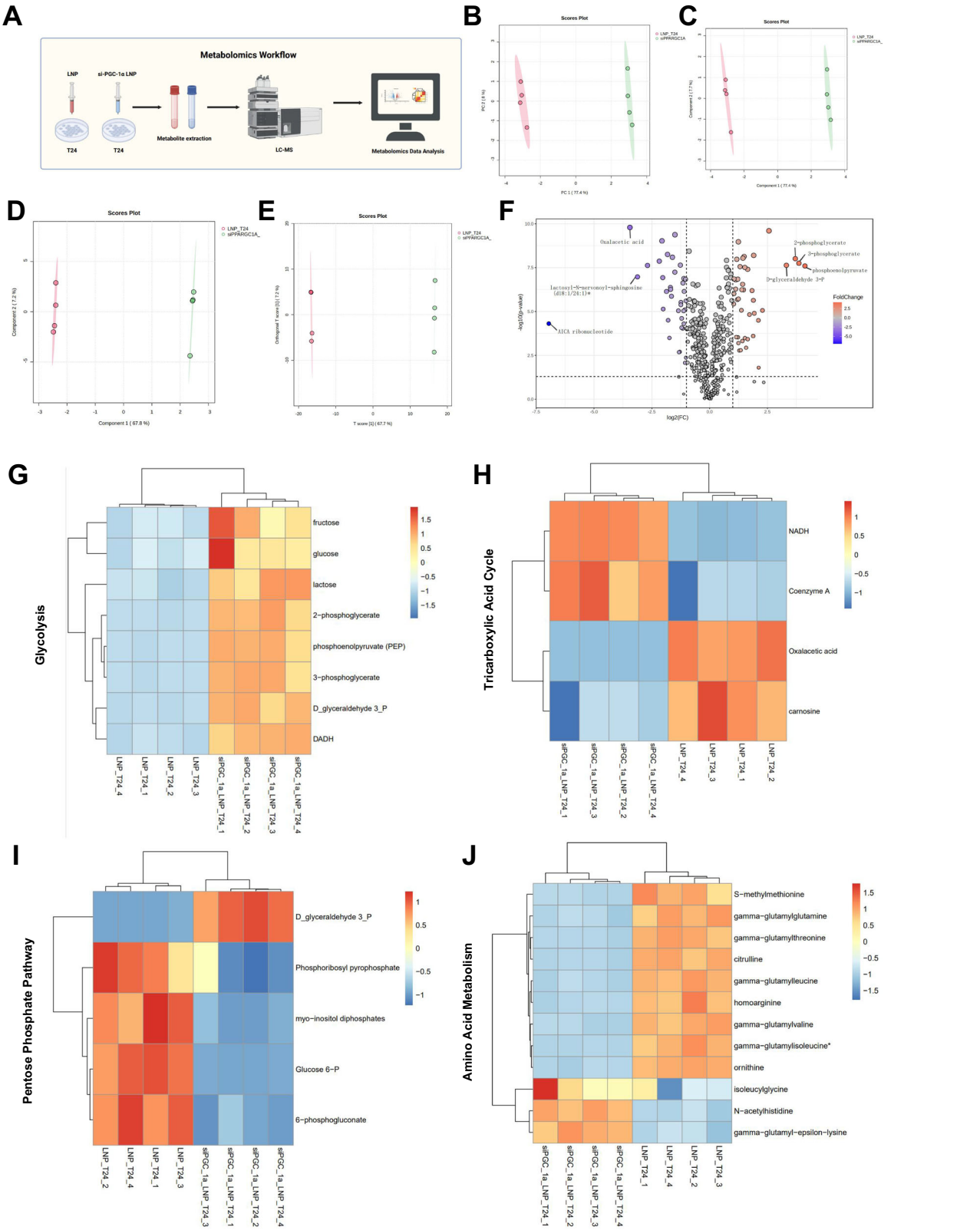

Fig. 4 | Analysis of the impact of si-PGC-1α LNP on T24 cell metabolism. **A** Workflow diagram for the Metabolomics study, including sample preparation, metabolite extraction, LC-MS analysis, and data analysis steps (created by BioRender); (**B**–**E**) Multivariate statistical methods were used to demonstrate the differences between the two cell groups in terms of metabolites, including PCA, Partial Least Squares Discriminant Analysis (PLSDA), Sparse Partial Least Squares Discriminant Analysis (sPLSDA), and Orthogonal Partial Least Squares Discriminant Analysis (OrthoPLSDA); (**F**) A volcano plot displays differential expression of metabolites, where gray dots represent metabolites with no significant difference, blue dots represent significantly downregulated metabolites, and red dots represent significantly upregulated metabolites; (**G**–**J**) Heatmaps depict the expression patterns of different metabolites involved in glycolysis, citric acid cycle, pentose phosphate pathway, and amino acid metabolism pathways, where red represents upregulation and blue represents downregulation; each group in the metabolome analysis consisted of four samples.

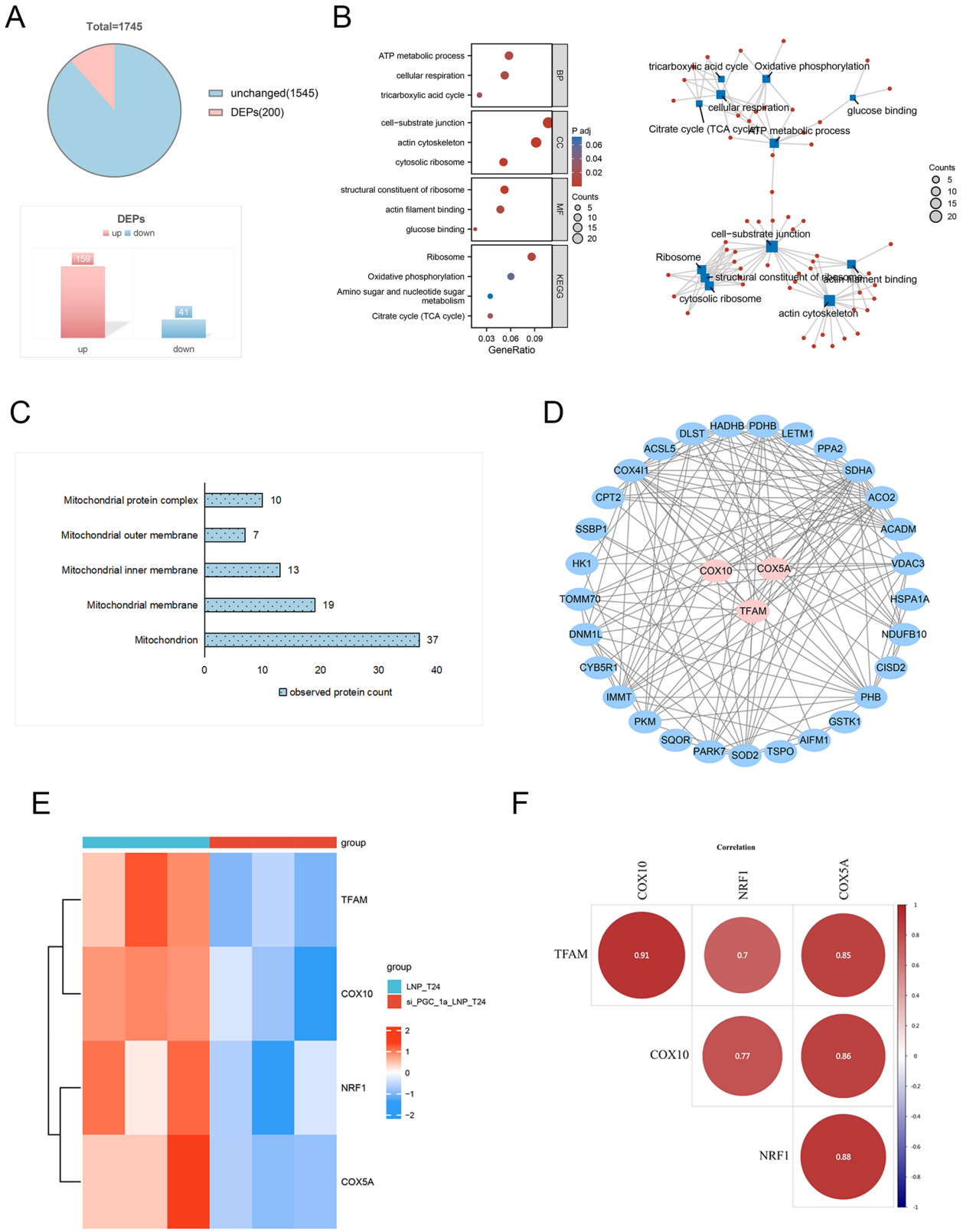

Fig. 5 | Proteomics analysis of cell samples from the LNP_T24 group and si-PGC-1α LNP_T24 group. A The pie chart illustrates the distribution of DEPs in the LNP_T24 group ($n = 3$) and si-PGC-1α LNP_T24 group ($n = 3$). The bar graph compares the number of upregulated and downregulated DEPs, with red representing upregulated proteins and blue representing downregulated proteins; (**B**) Enrichment analysis of DEPs using GO/KEGG, with circle color indicating the significance level of enrichment and circle size indicating the number of enriched genes. BP represents Biological Process, CC represents Cellular Component, and MF represents Molecular Function. The network diagram shows the correlation between various enrichment terms; (**C**) Bar graph displaying the mitochondrial localization of DEPs; (**D**) PPI network analysis of DEPs with mitochondrial localization, showing the interactions between these proteins; (**E**) Heatmap illustrating the protein expression of NRF1, TFAM, COX10, and COX5A; (**F**) Heatmap showing the correlation between NRF1, TFAM, COX10, and COX5A.

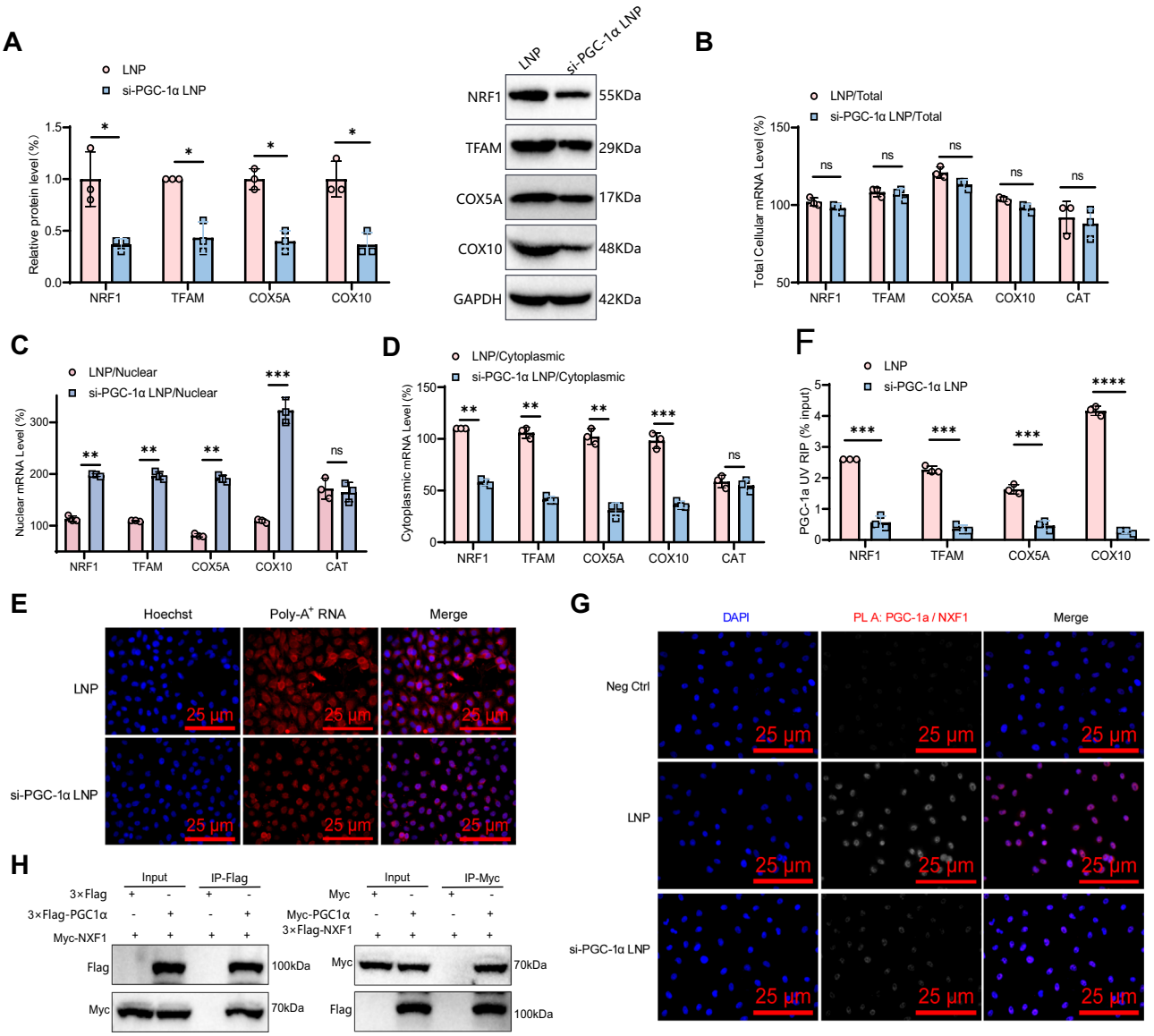

Fig. 6 | Analysis of the impact of si-PGC-1α LNP treatment on intracellular mRNA nuclear-cytoplasmic transport in T24 cells. A Western blot analysis of the expression levels of NXF1, NRF1, TFAM, COX10, and COX5A proteins in the two cell groups; (**B**–**D**) qRT-PCR analysis of the expression levels of NRF1, TFAM, COX10, COX5A and CAT mRNA in the total cell, nuclear, and cytoplasmic fractions of the two cell groups; (**E**) Cy3-dT FISH experiment analyzing the distribution of RNA in the two cell groups, with the bar equaling 25 μm (400×); (**F**) RIP experiment studying the binding of PGC-1α with target mRNA; (**G**) Proximity ligation assay (PLA) investigating the interaction between PGC-1α and NXF1, with the bar equaling 25 μm (400×); (**H**) CO-IP experiment exploring the interaction between PGC-1α and NXF1. All data are presented in the form of mean ± standard deviation. $^{*}P < 0.05$, $^{**}P < 0.01$, $^{***}P < 0.001$, $^{****}P < 0.0001$, while "ns" represents no significant difference ($P > 0.05$). Cell experiments were performed in triplicate.

Unencapsulated si-PGC-1α, LNP, and phosphate-buffered saline (PBS) were used as controls.

The results (Fig. 7A) showed that compared to the unencapsulated si-PGC-1α group, a stronger fluorescence signal was observed in the tumor tissue at 0.5 h after si-PGC-1α LNP injection. Moreover, the fluorescence distribution area in the si-PGC-1α LNP treated group was significantly larger than in the unencapsulated si-PGC-1α treated group. This suggests that si-PGC-1α carried by LNP exhibits superior tissue penetration within the tumor and has a more extensive distribution compared to the unencapsulated si-PGC-1α group.

At 16 h post-injection, the si-PGC-1α LNP group still showed a very strong fluorescence signal in the tumor tissue, while the unencapsulated si-PGC-1α group displayed a relatively noticeable fluorescence signal. In contrast, no significant fluorescence signal was observed in the LNP or PBS-treated groups. We speculate that LNP-encapsulated si-PGC-1α prevents nanoparticle aggregation and nonspecific protein adsorption within the tumor tissue, allowing si-PGC-1α LNP to remain at the tumor site longer than unencapsulated si-PGC-1α. These results indicate that si-PGC-1α LNP exhibits excellent distribution and penetration in tumor tissue.

Our study aimed to investigate whether si-PGC-1α encapsulated in LNP can reach tumor sites through the bloodstream and remain stable during circulation. To do so, we injected nude mice with PBS, unencapsulated si-PGC-1α, LNP, or si-PGC-1α LNP via the tail vein. After 6 h, we used the Xenogen IVIS Lumina system to detect the distribution of these complexes within the nude mice.

As shown in Fig. 7B, the si-PGC-1α LNP injection group exhibited an accumulation of si-PGC-1α LNP complexes in the heart, lungs, liver, kidneys, spleen, and particularly the tumors. In contrast, only background fluorescence in the tumors was observed in the si-PGC-1α injection group, indicating rapid removal of siRNA from the body in the absence of

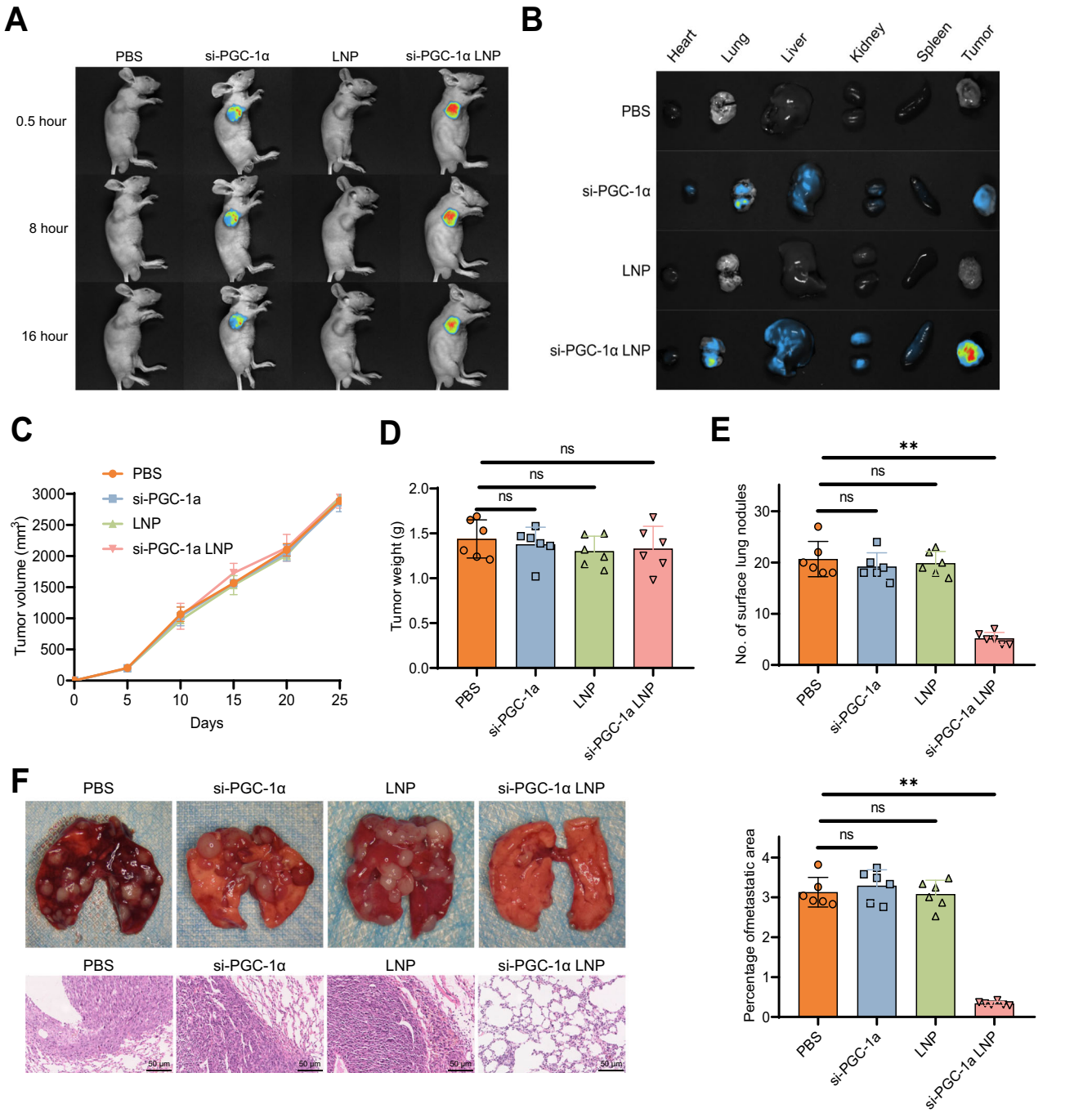

Fig. 7 | Analysis of the anti-tumor efficacy of si-PGC-1α LNP complexes. A In vivo imaging was performed after intravenous injection of PBS, unencapsulated si-PGC-1α4, LNP, or si-PGC-1α LNP in T24 xenograft nude mice ($n = 3$ per group). The bar in the figure represents 5 cm; (**B**) In vivo imaging was conducted in T24 xenograft nude mice after intravenous injection of PBS, unencapsulated si-PGC-1α4, LNP, or si-PGC-1α LNP ($n = 3$ per group). The bar in the figure represents 1 cm; (**C**) Tumor volume in the orthotopic bladder cancer model was measured after treatment with PBS, unencapsulated si-PGC-1α4, LNP, or si-PGC-1α LNP ($n = 6$ per group); (**D**) Tumor weight in the orthotopic bladder cancer model was measured after treatment with PBS, unencapsulated si-PGC-1α4, LNP, or si-PGC-1α LNP ($n = 6$ per group); (**E**) The number of lung tumor nodules in the mouse model of pulmonary metastasis was quantified after treatment with PBS, unencapsulated si-PGC-1α4, LNP, or si-PGC-1α LNP ($n = 6$ per group); (**F**) Lung nodules were identified using arrows in the tail vein injection of the pulmonary metastasis model, and the scale bar in the figure represents 20 mm. The lung tissue was stained with H&E (bottom). The scale bar in the histological image represents 50 μm (200×). The quantification of lung metastatic nodules in T24 tumor-bearing nude mice was shown on the right ($n = 6$ per group). All data are presented in the form of mean ± standard deviation. $^{**}P < 0.01$, while "ns" denotes no significant difference, which means $P > 0.05$.

nanoparticle encapsulation. These findings suggest that si-PGC-1α LNP is stable in circulation and can efficiently deliver to tumor sites through tail vein injection.

To assess the clinical significance of si-PGC-1α LNP complexes, we investigated their tumor suppressive effect in an in situ bladder cancer model, as intravesical chemotherapy is one of the main treatment methods for bladder cancer[35]. We successfully established an in situ bladder cancer model in rats and evaluated the anti-tumor effects of PBS, unencapsulated si-PGC-1α, LNP, or si-PGC-1α LNP. However, we did not observe any significant differences in tumor area or weight between the treatment groups (Fig. 7C, D), suggesting that si-PGC-1α LNP had no substantial therapeutic effect on in situ bladder tumors.

Additionally, we employed a BALB/c nude mouse model by injecting T24 cells into the tail vein to induce the formation of metastatic lung tumors. We quantified the number of lung metastatic nodules in the excised lung tissues from each treatment group. Compared to the PBS control group, unencapsulated si-PGC-1α, and LNP groups, nude mice treated with si-PGC-1α LNP showed a significant reduction in the number of lung metastatic nodules (Fig. 7E, F). Moreover, histological examination of lung tissue sections stained with H&E revealed that si-PGC-1α LNP had a remarkable inhibitory effect on the formation of macroscopic and microscopic metastatic lesions in the lungs when compared to the other treatment groups (Fig. 7F).

In summary, these results clearly demonstrate the significant antitumor metastatic effect of si-PGC-1α LNP, highlighting the potential of this nanoparticle-based delivery system in clinical applications.

Discussion

The present study aims to investigate the impact of liposomal nanoparticles delivering PGC-1α siRNA on cancer cells through transcriptome, proteome, and metabolome technologies in order to reveal its regulatory role in cancer cell reprogramming and energy metabolism and provide clues for the molecular mechanisms of metastatic bladder cancer treatment. A novelty of this study lies in the comprehensive analysis of the function and regulatory mechanisms of PGC-1α at multiple levels, offering new strategic directions for the treatment of metastatic bladder cancer.

Of particular interest, our analysis indicates that multiple differentially expressed genes are associated with the regulation of mitochondrial function. In the development of bladder cancer, mitochondria play a crucial role as the cellular powerhouses[36]. They are not only central to biological metabolism and energy production but also play a key role in the metabolic abnormalities that occur in the oxidative phosphorylation and glycolysis processes of cancer cells[36]. These metabolic changes may directly impact the energy production of tumor cells, thereby being correlated with their invasive and metastatic capabilities[37,38]. Changes in mitochondrial dynamics may be an adaptive response of tumor cells to environmental stressors such as acidosis and hypoxia, which are closely related to the disruption of mitochondrial function[39]. Particularly in bladder cancer, alterations in mitochondrial dynamics are not only associated with the migratory and invasive abilities of tumor cells but also likely serve as key driving factors for tumor cell metastasis from the primary site to other tissues.

The role of PGC-1α in cancer progression has been previously reported. Interestingly, it functions differently in various tumors. For example, PGC-1α can promote breast cancer cell invasion and metastasis by regulating mitochondrial biogenesis and oxidative phosphorylation[20,40], enhance gastric cancer cell proliferation and metastasis via the SNAI1/miR-128b axis, and drive in vitro and in vivo metastasis in cholangiocarcinoma by reversing the Warburg effect[41]. Conversely, PGC-1α inhibits liver cancer cell metastasis by suppressing aerobic glycolysis through the downstream target PDK1 in the WNT/β-catenin pathway[42]. Dual roles have been reported in melanoma and prostate cancer. In melanoma, it can both promote cell proliferation[43,44] and inhibit invasion through the ID2-TCF4-integrin signaling pathway[45]. In prostate cancer, PGC-1α can promote tumor growth via androgen receptor activation while inhibiting invasion and metastasis through its interaction with estrogen-related receptor α[46–48].

Previous studies have explored the application of transcriptome, proteome, and metabolome technologies in cancer cell metabolic reprogramming and metastasis[49–53]. However, compared to previous studies, this research provides a siRNA targeting method against PGC-1α with high delivery efficiency through transcriptome screening and the construction of a liposomal nanoparticles delivery system[54–56]. Furthermore, the research results concerning mitochondrial biology and energy metabolism further elucidate the significant role of PGC-1α[57,58]. Research highlights that PGC-1α's interaction with RNA/NXF1 is essential for the export of certain mitochondrial-related genes and mitochondrial homeostasis[59]. Thus, regulating the PGC-1α/NXF1 interaction can impact metabolic reprogramming and metastasis in cancer cells.

Based on transcriptome analysis, this study reveals significant differences in the metabolic processes between MBCCs and PBCCs, particularly the significant upregulation of PGC-1α expression in metastatic cells[60–62]. These results are consistent with previous studies, further validating the importance of PGC-1α in cancer cell energy metabolism reprogramming[63,64].

The efficient delivery of PGC-1α siRNA to bladder cancer cells was achieved through the liposomal nanoparticles delivery system in this study, resulting in significant downregulation of the PGC-1α protein levels. Moreover, the accumulation of PGC-1α mRNA in the nucleus and the inhibition of mitochondrial biology and energy metabolism indicate the significant impact of PGC-1α siRNA delivery on cancer cell function.

Through the detection of mitochondrial DNA content, ATP levels, mitochondrial morphology and quantity, and relative OC, this study reveals the inhibitory effect of PGC-1α siRNA delivery on cancer cell mitochondrial biology and energy metabolism. These changes, closely related to mitochondrial function, demonstrate the importance of PGC-1α in regulating energy metabolism processes[65–67].

In conclusion, our study suggests that si-PGC-1α LNP effectively halts bladder cancer growth and metastasis by inhibiting mitochondrial biogenesis and energy metabolism processes in cancer cells. The silencing of PGC-1α mediated by si-PGC-1α LNP not only plays a crucial role in cancer cell energy metabolism but also impacts tumor metastasis, providing new perspectives for understanding bladder cancer metastasis mechanisms.

The scientific and clinical value of this research lies in exploring the effects of liposomal nanoparticle-delivered PGC-1α siRNA on cancer cells and revealing its regulatory role in cancer cell reprogramming and energy metabolism. Through a combined application of transcriptomics, proteomics, and metabolomics, we observed PGC-1α overexpression in MBCCs and demonstrated that PGC-1α silencing inhibits cancer cell energy metabolism and metastatic potential. This work offers essential clues for uncovering molecular mechanisms for metastatic bladder cancer therapy and lays the foundation for novel therapeutic strategies and targeted drugs.

However, this study has limitations, being based on cell lines and mouse models. Further validation in human models is required to confirm the feasibility and effectiveness of these findings. Additionally, our research mainly focused on the regulatory role of PGC-1α, potentially overlooking other molecular mechanisms involved. This study also centered on PGC-1α's impact on mitochondrial biogenesis, while disregarding effects on mitophagy. Electron microscopy images in Fig. 3F show mitochondrial swelling in the si-PGC1α group, suggesting that dysfunctional mitochondria accumulation may result from decreased autophagy. Research indicates that while PGC-1α regulates mitochondrial biogenesis, it also influences functions beyond biogenesis, including mitochondrial quality control processes such as fusion, fission, and mitophagy. PGC-1α significantly promotes autophagy, particularly mitophagy[68–70]. Future research could explore PGC-1α interactions with other molecules, pathways, and cellular signaling processes.

PGC-1α regulates the transcriptional activity of target genes in response to environmental stimuli, including hormones, growth factors, fasting/feeding shifts, exercise, and temperature fluctuations[70–73]. By interacting with transcription factors or indirectly activating these regulators, PGC-1α enables cells to adapt to metabolic demands and supports mitochondrial biogenesis[74,75]. In brown adipose tissue (BAT), prolonged cold exposure activates the β-adrenergic signaling pathway, which triggers post-translational modifications activating PGC-1α, thereby enhancing PGC-1α gene expression[76–78]. Consequently, PGC-1α activates NRF1 and PPARγ, driving mitochondrial biogenesis and adaptive metabolism, leading to metabolic reprogramming. The roles of PGC-1α and its target genes in diverse cellular environments remain incompletely understood, meriting further in-depth exploration in future studies.

Gene silencing has been proposed as a therapeutic approach, with siRNA offering promising silencing mechanisms. However, delivering

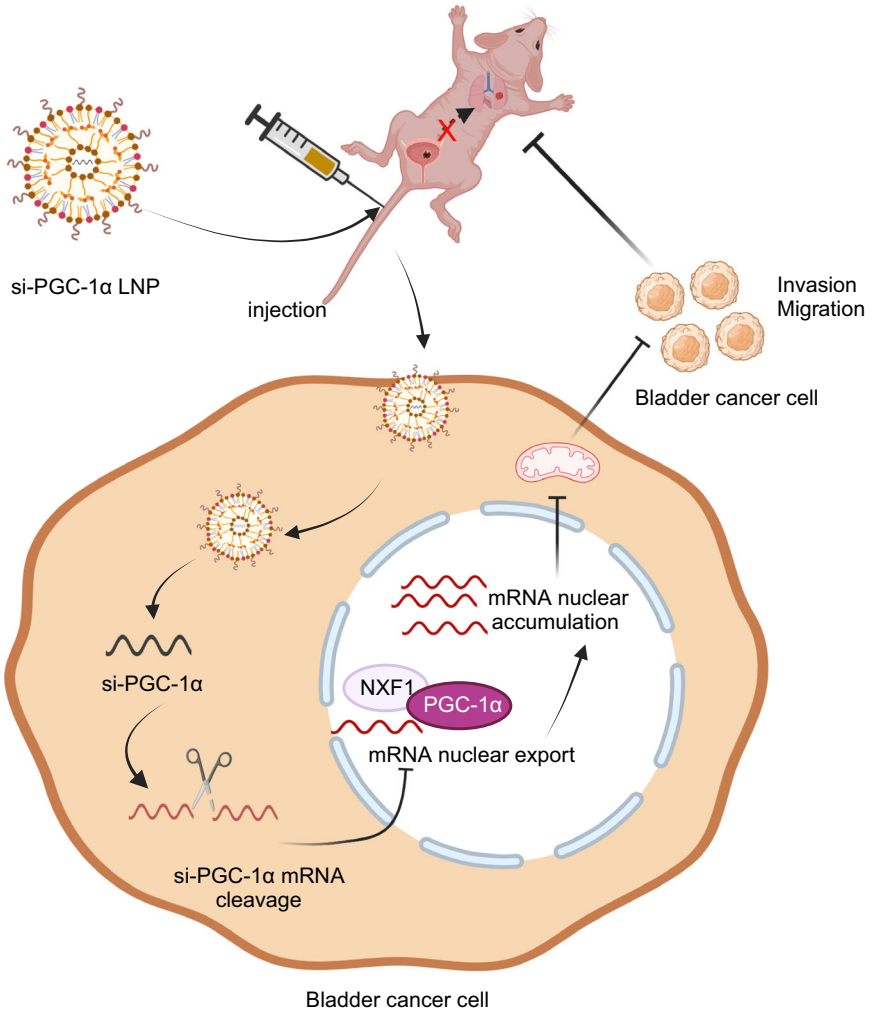

Fig. 8 | Schematic representation of the molecular mechanism underlying the inhibition of mitochondrial biology and energy metabolism regulation in bladder cancer metastasis by si-PGC-1α LNP (created by BioRender). Silencing PGC-1α via siRNA-loaded liposomal nanoparticles disrupts mitochondrial biogenesis and energy metabolism in bladder cancer cells, leading to impaired oxidative phosphorylation, reduced ATP production, and altered mitochondrial morphology. Additionally, PGC-1α silencing hinders nuclear-cytoplasmic mRNA export through interference with NXF1 interaction, contributing to transcriptional dysregulation. These molecular alterations suppress cancer cell invasion, migration, and metastatic potential, highlighting the therapeutic potential of nanoparticle-mediated PGC-1α targeting in metastatic bladder cancer.

siRNA into cells to specific tissues and target organs remains challenging due to stability and specificity considerations, as well as delivery system requirements[79]. This limits the potential for using NC-siRNA as a control in target gene-siRNA studies.

Future research directions include developing more targeted and efficient nanoparticle delivery systems for PGC-1α, further verifying therapeutic efficacy for metastatic bladder cancer, and exploring combinations with other treatments such as chemotherapy, immunotherapy, or radiotherapy for enhanced therapeutic outcomes. Traditional cancer treatments, combining surgery, chemotherapy, and radiotherapy, lack targeting specificity, often affecting normal cells and causing severe adverse reactions, thus limiting their clinical applications. Immunotherapy provides new hope for bladder cancer treatment, offering higher specificity and relatively fewer side effects, albeit with certain limitations. Bacillus Calmette-Guerin (BCG) is a classic immunotherapy for bladder cancer, widely used in postoperative instillation. BCG activates $CD4^+$ and $CD8^+$ T cells, producing cytokines like IL-2 and IL-12, promoting Th0 to Th1 differentiation, and inducing T cell activation and proliferation for cell-specific immunity. BCG also induces TLRs and activates monocytes to release IL-12 and IFN-α, thereby activating NK cells to directly kill tumor cells[80]. However, BCG is associated with severe adverse effects, including acute toxicities (dysuria, hematuria, fever, bladder irritation) and delayed toxicities (flu-like symptoms, pneumonia, hepatitis, granulomatous prostatitis)[81]. This study's direct intratumoral injection of si-PGC-1α LNP demonstrates high specificity, unlike chemotherapy, significantly reducing adverse reactions (Fig. 8).

Materials and methods

Animal ethics

Our research adheres strictly to international, national, and local laws and has gained approval from the Institutional Animal Care and Use Committee. We consistently prioritize the welfare of animals, striving to minimize their pain and discomfort. We provide appropriate housing conditions, ample food, and water, and we implement professional anesthesia and pain relief measures. All procedures involving animals are conducted under the guidance of veterinary experts. Researchers have undergone training and certification to ensure proper handling and care of the animals. At the conclusion of experiments, we employ humane euthanasia methods to ensure they are relieved from any suffering. These ethical principles and practices guarantee the respect and protection of animals in our research[82].

Sample collection, transcriptome sequencing, and data quality control

Sample Collection: Three female BALB/c nude mice (8 weeks old, weighing an average of 24 ± 3 grams) were obtained from Vitens Co., Ltd., Beijing, China. A T24 cell line carrying a GFP tag (1×10^6, 100 μl) was injected into the bladders of all nude mice to induce the formation of metastatic bladder cancer. In situ, bladder cancer samples were collected at week 10. Tumor development was evaluated between week 10 and week 16 using computer tomography (CT) scans. Lung metastasis bladder cancer samples were collected at week 16 for histological examination to confirm the successful establishment of tumors. Tumor tissue samples were processed into cell

suspensions and GFP-positive cells were sorted using flow cytometry for subsequent analysis[83].

RNA extraction from cells was performed using Trizol reagent (16096020, Thermo, USA). The concentration, purity, and integrity of RNA were measured using the Qubit® 2.0 Fluorometer® (Q33216, Life Technologies, USA) with the Qubit® RNA Assay Kit (HKR2106-01, Shanghai Baoji Biotechnology Co., Ltd., China), Nanometer spectrophotometer (IMPLEN, USA), and Bioanalyzer 2100 system with the RNA Nano 6000 Assay Kit (5067-1511, Agilent, USA), respectively.

A total of 3 μg of RNA from each sample was used as the input material for RNA sample preparation. Following the manufacturer's instructions, the NEBNext® Ultra™ RNA Library Prep Kit (E7435L, NEB, Beijing, China) compatible with Illumina® (USA) was used to generate cDNA libraries, with library quality evaluated on the Agilent Bioanalyzer 2100 system. Using the TruSeq PE Cluster Kit v3 cBot HS (Illumina) (PE-401-3001, Illumina, USA), indexed samples were clustered on the cBot cluster generation system. After cluster generation, the libraries were sequenced on the Illumina HiSeq 550 platform, generating 125 bp/150 bp paired-end reads[84,85].

Quality assessment of the raw sequencing data was performed using FastQC software v0.11.8 to examine the quality of paired-end reads. Cutadapt software 1.18 was utilized for initial data preprocessing, including the removal of Illumina sequencing adapters and poly(A) tail sequences. Perl scripts were employed to filter out reads with N content exceeding 5%. The FASTX Toolkit software 0.0.13 was used to extract reads with a base quality of 20 or above, which accounted for 70% of the total bases.

BBMap software was employed for repairing paired-end sequences. Finally, the filtered high-quality read fragments were aligned with the human or mouse reference genome using hisat2 software (0.7.12).

The transcriptome sequencing data were analyzed using the Xiantao Academic Online Analysis Tool[86,87].

Hematoxylin and eosin (H&E) staining

To begin, tissue samples were fixed in 4% paraformaldehyde (P0099-100 ml, beyotime, Shanghai, China) for 24 h to preserve tissue structure. Afterward, the fixed samples underwent dehydration using a series of alcohol solutions with increasing concentrations, followed by clarification with xylene (X112050-5 ml, Aladdin, Shanghai, China). Subsequently, the processed tissue samples were embedded in paraffin and cut into thin sections of 4-5 micrometers thickness using a microtome.

Once sectioning was complete, paraffin was removed with xylene, and then the sections were rehydrated with alcohol solutions of decreasing concentrations. Afterward, the sections were stained separately with hematoxylin (H432819-25g, Aladdin, Shanghai, China) and eosin (E301878-500ml, Aladdin, Shanghai, China) to stain the cell nuclei and cytoplasm, respectively.

Following staining, the sections were dehydrated again using a series of alcohol solutions, cleaned with a clearing agent, and then mounted with a mounting medium and coverslip. Finally, the stained tissue sections were observed and analyzed under an optical microscope to identify and evaluate the characteristics and metastatic status of the tumor tissue.

Immunofluorescence staining

The sample collection process was carried out as follows: Firstly, primary bladder cancer cells (PBCCs) and metastatic bladder cancer cells (MBCCs) expressing GFP were selected from bladder cancer tissue using flow cytometry. Subsequently, these cells were prepared as cell slides and fixed with 4% paraformaldehyde solution (P0099-100ml, beyotime, Shanghai, China) for 15–20 min. Following this, cell permeabilization was performed using a PBS solution containing Triton X-100, and a blocking solution with BSA was applied to reduce nonspecific binding.

Next, a primary antibody against PGC-1α (66369-1-Ig, Proteintech, USA/) was diluted to a concentration of 1:200 and incubated on the cell slides overnight at 4 °C. After incubation, the slides were washed with PBS to remove the unbound primary antibody and then incubated with a fluorescently labeled secondary antibody (A-21065, thermofisher, USA) at a concentration of 1 μg/mL.

DAPI fluorescent dye (C1005, beyotime, Shanghai, China) was used to stain the cell nuclei. Finally, the slides were washed and covered with an anti-fading mounting solution (P0131-25 ml, beyotime, Shanghai, China). The fluorescence signals were observed and captured using a Leica SP8 confocal microscope, with 3 fields of view captured for each sample. The fluorescence intensity was quantified using Leica SP8 image analysis software to compare the expression difference of PGC-1α in PBCCs and MBCCs[20].

Preparation and characterization of si-PGC-1α lipid nanoparticle (LNP)

Preparation of FAM-labeled PGC-1α siRNA: The sequence provided in Table S1[34] was used for the synthesis of FAM-labeled PGC-1α siRNA. The FAM label was attached to the 5' end of the siRNA for fluorescence detection. Additionally, "tt" modifications were added to the 3' end to enhance siRNA stability and efficiency. The single-stranded RNA was produced by Kingsray Biotechnology Co., Ltd., located in Nanjing, China.

Preparation of LNPs (Fig. S3): DLin-KC2-DMA (S87825, Shanghai Yuan Ye Biotech, Shanghai, China), DSPC (S50960, Shanghai Yuan Ye Biotech, Shanghai, China), cholesterol (A10076, Shanghai Yuan Ye Biotech, Shanghai, China), and PEG–DMG (S22698, Shanghai Yuan Ye Biotech, Shanghai, China) were dissolved in ethanol (R433208-1L, Aladdin, Shanghai, China). These components were mixed in a molar ratio of approximately 50:10:38.5:1.5 (DLin-KC2-DMA:DSPC:cholesterol: PEG–DMG), referred to as the LNP09 formulation. The lipid mixture was then added to 50 mM citric acid (pH 4) (C434173-100g, Aladdin, Shanghai, China) to generate a solution containing 30% ethanol.

Subsequently, the obtained solution was extruded through a 0.05 μm pore size membrane (FPB005A12, Membrane Solutions, Shanghai, China) and mixed with si-PGC-1α prepared in 30% ethanol and 50 mM citric acid (pH 4) to achieve a total lipid:siRNA ratio of approximately 7:1 (by weight). Ethanol was removed, and the mixture was replaced with a buffer containing PBS (pH 7.5) containing 155 mM NaCl (S433750-100g, Aladdin, Shanghai, China), 3 mM Na2HPO4 (S118442-500g, Aladdin, Shanghai, China), and 1 mM KH2PO4 (P113042-500g, Aladdin, Shanghai, China) through dialysis.

The final formulation was filtered through a 0.22 μm filter (FF372-10pcs, Beyotime, Shanghai, China) and adjusted to a final concentration of approximately 1 mg/ml using PBS. The particle size was determined using a Malvern Zetasizer NanoZS (Malvern, UK). The nanoparticle content of siRNA was validated using ion exchange HPLC and DNAPac PA200 column (Dionex Corporation, Sunnyvale, USA). The morphology of LNP was observed using transmission electron microscopy (JEOL 100CX II TEM, Japan). Particle size and zeta potential were measured using Malvern Zetasizer Nano ZS[83].

Analysis of si-PGC-1α LNP uptake rate

In this experiment, two groups were established: ① Control group: T24 cell line co-incubated with FAM-labeled PGC-1α siRNA, and ② Experimental group: T24 cell line co-incubated with liposome nanomaterials delivering FAM-labeled PGC-1α siRNA. The concentration of siRNA in each experimental group was 200 nM.

Initially, the T24 human bladder cancer cell line was cultured in a six-well tissue culture plate. Subsequently, depending on the experimental grouping, FAM-labeled PGC-1α siRNA or liposome nanomaterials delivering FAM-labeled PGC-1α siRNA were added. The cells were then incubated for 3 h at 37 °C and 5% CO_2, followed by two washes with 1× PBS to remove non-internalized siRNA or liposomes.

For confocal microscopy analysis, cells were fixed with 4% paraformaldehyde (P0099-100 ml, beyotime, Shanghai, China) to preserve cell morphology. DAPI staining (C1005, beyotime, Shanghai, China) was used to visualize the position of cell nuclei. Finally, cells were observed using a Leica TCS SP8 confocal laser scanning microscope, acquiring images using

an excitation wavelength of 488 nm with FITC emission wavelength between 500 and 580 and DAPI emission wavelength between 405 nm and 410–490 nm. Image analysis was performed using LAS AF software to obtain data regarding siRNA uptake rate[88].

For flow cytometry analysis, cells were detached from the culture plate using 0.25% trypsin/0.53 mM EDTA solution (25200056, thermofisher, USA) to obtain a single-cell suspension. Afterward, the separated cells were collected by centrifugation to remove colloids and other impurities. Flow cytometry analysis was performed using a BD FACSCanto™ II to measure the uptake rate of cells using the fluorescence signal of FAM-labeled PGC-1α siRNA. The flow cytometer detected the FAM-labeled signal and determined the number of positive cells as well as the intensity of the fluorescence signal. Finally, the siRNA uptake rate was calculated by analyzing the data collected by the flow cytometer[88]. The gating strategy can be seen in Fig. S5.

Cell culturing

The T24 human bladder cancer cell line (Bio-73168, Chinese Microbial Culture Collection, Beijing, China) was obtained from the Chinese Microbial Culture Collection. All bladder cancer cell lines were cultured in RPMI-1640 medium (11875093, Thermo Fisher, USA), supplemented with 10% fetal bovine serum (FBS) (10099-141, Gibco, USA), 100 U/mL penicillin, and 100 mg/mL streptomycin (15140122, Thermo Fisher, USA).

These cell lines were cultured at 37 degrees Celsius in a humidified atmosphere containing 5% CO_2[89].

Cell transfection and other treatments

In this study, T24 cells were grouped as follows: GFP expression group, Flag and 13myc-tagged protein expression group, and PGC-1α::Flag and NXF1::13myc fusion protein expression group. The expression of target proteins was achieved through lentiviral transfection. Plasmids and lentiviral packaging services were provided by JIKAI Gene (Zhejiang, China). GV208 vector (GV208, GeneChem, Zhejiang, China) was used for gene expression experiments, and the desired fragments were successfully cloned into the AgeI site. Additionally, in order to monitor the activity of the relevant genes, the luciferase reporter plasmids were co-transfected with helper plasmids into 293 T cells (catalog number: CRL-3216, ATCC, USA), and packaged lentivirus was obtained after validation, amplification, and purification.

For lentivirus-mediated cell transfection, 5×10^5 cells were seeded into a 6-well plate. When the cells reached 70–90% confluency, the medium containing an appropriate amount of packaged lentivirus (MOI = 10, working titer approximately 5×10^6 TU/mL) and 5 μg/mL polybrene (Merck, TR-1003, USA) was added for transfection. After 4 h of transfection, an equal amount of medium was added to dilute polybrene, and after 24 h of transfection, a fresh medium was replaced. The cells were selected with 1 μg/mL puromycin (Thermo Fisher, A1113803, USA) for 2 weeks to obtain stably transfected cell lines[90].

All the lentiviral vectors mentioned above were designed and synthesized by JIKAI Gene.

Western blot analysis

Cells from different groups were collected and lysed on ice using RIPA lysis buffer (P0013B, Beyotime, Shanghai, China) supplemented with 1% PMSF for 30 min. The lysates were then centrifuged at 14,000 *g* and 4 °C, and the supernatant was collected. The protein concentration in the samples was determined using the BCA method (P0012S, Beyotime, Shanghai, China). An appropriate amount of 5× loading buffer was added to the protein extract, followed by boiling at 100 °C for 10 min to denature the proteins. A total of 50 μg of protein was loaded onto the SDS-PAGE gel for electrophoresis. After electrophoresis, the protein bands containing the target protein were transferred onto a PVDF membrane (FFP24, Beyotime, Shanghai, China).

The PVDF membrane was then incubated in 5% skim milk powder at room temperature for 1 h. Subsequently, the membrane was incubated overnight at 4 °C with primary antibodies, including anti-PGC-1α antibody (rabbit; 1:1000, AF7736, Beyotime, Shanghai, China), anti-nuclear respiratory factor 1 (NRF1) antibody (rabbit; 1:1000, AF5298, Jiangsu Procell Biological Technology, Jiangsu, China), anti-TFAM antibody (rabbit; 1:1000, AF0531, Jiangsu Procell Biological Technology, Jiangsu, China), anti-cytochrome C oxidase subunit 5a (COX5A) antibody (rabbit; 1:1000, DF3561, Jiangsu Procell Biological Technology, Jiangsu, China), anti-cytochrome c oxidase assembly protein (COX10) antibody (rabbit; 1:1000, DF8524, Jiangsu Procell Biological Technology, Jiangsu, China), and anti-β-Actin antibody (rabbit; 1:5000, AF7018, Jiangsu Procell Biological Technology, Jiangsu, China).

β-Actin was used as an internal control. After washing with PBST buffer at room temperature, the membrane was incubated with horseradish peroxidase (HRP)-conjugated goat anti-rabbit IgG secondary antibody (1:10,000, BA1054, Boster, Wuhan, China) at room temperature for 1 h. The membrane was washed six times with PBST buffer for 5 min each time. The ECL reaction solution (AR1172, Boster, Wuhan, China) was evenly applied onto the membrane, and it was then exposed to an imaging system (Amersham Imager 600, USA). The grayscale analysis was performed using Image J software[91,92]. The experiment was repeated three times. Please refer to supplementary information for all uncut WB images (Fig. S6).

Measurement of mitochondrial DNA content

The experiment to measure mitochondrial DNA content consisted of two experimental groups: ① Control group: T24 cell line co-incubated with liposome nanomaterials and ② Treatment group: T24 cell line co-incubated with liposome nanomaterials delivering FAM-labeled PGC-1α siRNA. The latter group had a siRNA concentration of 200 nM in the incubation system. The T24 cell line, along with the corresponding liposome nanomaterials, was incubated for 8 h at 37 °C and 5% CO_2. Following incubation, the cells were washed twice with 1×PBS to remove any non-engulfed siRNA or liposomes.

Subsequently, total DNA was extracted from the cells, and the relative expression level of cytochrome c oxidase 1 (mtCO1) was analyzed through PCR to serve as a reference for measuring mitochondrial DNA content. In human samples, mtCO1 expression levels were compared with beta-globin expression levels[20]. The primer sequences used are detailed in Table S2.

Measurement of adenosine triphosphate (ATP) content

The measurement of ATP was performed using the ATP assay kit (S0026, Beyotime, Shanghai, China). Firstly, cells were centrifuged, and the supernatant was discarded. The pellet was then homogenized in lysis buffer and centrifuged at 12000 *g* for 5 min at 4 °C. The supernatant was collected for ATP measurement. Secondly, an ATP standard curve was prepared by diluting the ATP standard solution with ATP assay lysis buffer to different concentrations to match the ATP concentration in the samples. Next, the ATP assay working solution was prepared by diluting the ATP assay reagent at a ratio of 1:9. Finally, 100 μL of the ATP assay working solution was added to the wells, followed by the addition of 20 μL of the sample or standard solution. The relative light units (RLU) were then measured using a chemiluminescence reader or liquid scintillation counter[20].

TEM

First, the sample was fixed in 0.1 M Sorenson's buffer (MG5510, Meiji Biological, Shanghai, China) containing 2.5% glutaraldehyde (LM-1606D, Shanghai Unionmai Biological, Shanghai, China) for 3 h.

Next, the cells were treated with 1% OsO4 (20816-12-0, Ruifeng, Zhejiang, China) in 0.1 M Sorenson's buffer for 2 h. After treatment, the cells were stained with 1% tannic acid (1401-55-4, Ruifeng, Zhejiang, China) and subjected to an ethanol dehydration series, followed by embedding in Embed-812 (14120, Hyde Enterprise, Beijing, China).

Finally, thin sections were stained with 1% uranyl acetate (71767-12-9, Ruifeng, Zhejiang, China) and 0.4% lead citrate (512-26-5, Shanghai Guchen Biological, Shanghai, China), observed under a TEM-1400 Plus electron microscope at magnifications of 5000-50000x. Digital images were obtained using the AMT imaging system (Advanced Microscopy

Techniques). For quantitative analysis, 3-9 cells were examined for each group at a magnification of ×5000, and the number of mitochondria per cell in the slice image was calculated[20].

Determination of cellular oxygen consumption rate (OCR)

The OCR was measured using the Seahorse XF24 and XF96 instruments (Agilent) under standard conditions. Measurements were taken after adding 0.1 μM Oligomycin (MZ8002-1MG, Mochaon Biotech, Zhejiang, China), 0.05 μM FCCP (MX3259-100UL, Mochaon Biotech, Zhejiang, China), 1 μM Rotenone (MX7451-1G, Mochaon Biotech, Zhejiang, China), and 10 μM Atpenin A5 (HY-126653, MedChemExpress, USA). The OCR was measured in real-time, quantifying the picomoles of oxygen consumed per minute (pmol/min), and graphed over time, before and after the addition of Rotenone to the culture medium (baseline OCR and specifically used for measuring mitochondrial respiration).

The difference in OCR before and after the addition of Rotenone to the medium reflects the oxygen consumption by the mitochondria (mitochondrial OCR). The OCR measurements were adjusted based on the number of cells in each well of the cell culture plate. To achieve this, cells were fixed with 4% paraformaldehyde (P0099-100ml, Beyotime, Shanghai, China), permeabilized, stained with 0.1% crystal violet (G1064, Solarbio, Beijing, China), and measured using a plate reader (Molecular Devices) through spectrophotometry after the cells were dissolved with 10% acetic acid (A298827-500ml, Aladdin, Shanghai, China).

For OCR measurements in permeabilized cells, a cell membrane permeabilization reagent kit (102504-100, Agilent, USA) was used. Cells were permeabilized for 30 min and then supplemented with 10 mM malic acid (M433327-100g, Aladdin, Shanghai, China) and 10 mM glutamate (G103978-25g, Aladdin, Shanghai, China) in the culture medium. Subsequently, 4 mM ADP (60604ES03, Yeasen, Shanghai, China), 2 μM Rotenone, 10 mM succinic acid (S431423-250g, Aladdin, Shanghai, China), and 2.5 μM antimycin A (MSO070-10MG, Mochaon Biotech, Zhejiang, China) were sequentially injected[20].

Metabolome analysis

The sample collection process is as follows: firstly, T24 cell lines were co-cultured with FAM-labeled PGC-1α siRNA delivered by either liposome nanomaterials or liposome nanomaterials, with the concentration of the latter siRNA set to 200 nM. After incubating at 37 °C and 5% CO_2 for 8 h, the cells were washed twice with 1×PBS to remove any unabsorbed siRNA or liposomes. Each group consisted of four replicates, resulting in four samples per group. Subsequently, the metabolites were extracted by lysing the cells with the application of a metabolite extraction solution, which released the metabolites and separated them from cellular debris through a second centrifugation. Finally, the supernatant containing the metabolites was collected, dried, and reconstituted in an appropriate solvent for liquid chromatography-mass spectrometry (LC-MS) analysis.

The metabolite extract was dried into particles using SpeedVac without any heat applied throughout the process. Metabolomics analysis was performed using an LC20 HPLC system (Shimadzu, Japan) combined with a Triple TOF-6600 mass spectrometer (AB Sciex). Waters ACQUITY UPLC HSS T3 C18 column (100 × 2.1 mm, 1.8 μm) was selected for chromatographic separation. The column temperature was maintained at 40 °C, and elution was carried out at a flow rate of 0.4 mL/min. The mobile phase consisted of an acetonitrile-water solution containing 0.1% formic acid. The gradient elution program for mobile phase B was as follows: 5%, 0.0–11.0 min; 90%, 11.0-12.0 min; 5%, 12.1–14 min. The eluent was directly introduced into the mass spectrometer without splitting[93].

The mass spectrometry conditions were as follows: ionization voltage, 5500 V; capillary temperature, 550° C; nebulizer gas flow rate, 50 psi; auxiliary heating gas flow rate, 60 psi. Subsequent data processing and statistical analysis were conducted using Masslynx and Markerlynx XS software from Waters. The raw data obtained from UPLC-Q/TOF-MS analysis were preprocessed, including noise filtering, peak discrimination, peak alignment, and normalization, resulting in a three-dimensional matrix table containing retention time, mass-to-charge ratio, and peak intensity. The preprocessed three-dimensional matrix table was imported into SIMCA-P software (Umetrics, Umea, Sweden) for multivariate data analysis. Prior to pattern recognition analysis, Pareto scaling was applied to scale the data. Unsupervised principal component analysis (PCA), supervised partial least squares discriminant analysis (PLS-DA), and orthogonal partial least squares-discriminant analysis (OPLS-DA) were performed using the online tool MetaboAnalyst to analyze the data from the two groups[94,95].

Scratch healing experiment

Single-cell suspensions were prepared from well-growing cell groups using the aforementioned method. The cell suspensions (2 mL, 8×10^5 cells/mL) were seeded into a six-well plate. The cells were then cultured in a CO_2 incubator at 37 °C until reaching a growth density of 90–100%. A scratch was made on the cell monolayer using a 200 μL pipette tip perpendicular to the plate surface. The plate was washed with PBS to remove any floating cells, followed by the addition of a culture medium. After 24 h of further incubation, photographs were taken to calculate the scratch healing rate. The scratch healing rate was determined by the formula: (initial scratch width - final scratch width) / initial scratch width × 100%[96]. The experiment was repeated three times.

Invasion assay

The invasive ability of T24 cells was determined using a Transwell culture chamber (8 μm, SBM07797, Solelybio, Beijing, China). Matrigel (356234, Solarbio) was coated on the bottom of the Transwell upper chamber to simulate the in vivo matrix environment. A total of 5×10^4 cells of T24 cell suspension were added to each upper chamber of the Transwell system, with a volume of 200 μL. The Transwell system was then incubated at 37°C for 24 h. After incubation, the culture medium in the lower chamber of the Transwell was removed, and the system was washed with PBS buffer twice. Subsequently, the cells that did not migrate through the Transwell membrane were gently wiped off using a cotton swab. The remaining cells in the lower chamber were stained with 0.1% crystal violet solution (G1063, Solarbio) for 20 min. Finally, the stained T24 cells that passed through the membrane were counted under an optical microscope to assess their invasive ability[20].

Experiment on contraction of type I collagen

For the analysis of gel contraction ability in T24 cells, the Type I Collagen Reagent Kit (C8062, Solarbiop) from Solarbiop was used. Initially, the collagen was diluted to a concentration of 0.012 mg/mL and coated on the surface of the cell culture vessels at a density of 2 μg/cm². After coating, the vessels were allowed to air dry overnight or placed at room temperature for 1 h, followed by washing with PBS. Next, three-dimensional collagen gels, with or without cells, were prepared at a concentration of 2 mg/mL. The collagen solution was mixed with NaOH, PBS, or culture medium. Cell suspension was also added for collagen with cells. After mixing, the solution was immediately added to the culture vessels and left at room temperature for 20 min to allow gel solidification. The vessels were then transferred to an incubator for cultivation[97].

Preparation of protein samples

Initially, T24 cell lines were collected after co-incubation with liposome nanomaterials or liposome nanomaterials delivering FAM-labeled PGC-1α siRNA for 8 h. Then, a phenol extraction buffer containing 10 mM DTT (R0861, MBI, Beijing, China), 1% protease inhibitor mixture (P6731, Solarbio, Beijing, China), and 2 mM EDTA (E1170, Solarbio, Beijing, China) was used for ultrasonication using a sonic cell disruptor (SCIENTZ-IID, Scientz, Ningbo, China) under ice bath conditions. This step was repeated 8 times. Subsequently, an equal volume of Tris-saturated phenol (HC1380, Vander Biology, Beijing, China) at pH 8.0 was added, and the mixture was vortexed for 4 min. Then, the mixture was centrifuged at 5000 x *g* for 10 min at 4 °C, and the upper layer of phenol was transferred to a new centrifuge tube. To the phenol solution, 0.1 M ammonium sulfate

(101217, Merck, USA) saturated with methanol (106035, Merck, USA) in a volume ratio of 1:5 was added, and the mixture was left overnight to precipitate proteins. Afterward, the solution was centrifuged at 4 °C for 10 min to remove the supernatant. Finally, the remaining precipitate was washed once with ice-cold methanol and three times with ice-cold acetone. The washed protein was re-dissolved in 8 M urea (U8020, Solarbio, Beijing, China), and the protein concentration was determined using the BCA assay kit (P0012, Biyun Tian, Shanghai, China) according to the manufacturer's instructions[98].

Protease digestion, peptide labeling, and nano-LC-MS/MS analysis

Each sample was subjected to enzymatic digestion using 50 μg of protein. The protein solution was mixed with DTT to a final concentration of 5 mM and incubated at 56 °C for 30 min. Acetamide (A108460-25kg, Aladdin, Shanghai, China) was then added to achieve a concentration of 11 mM and incubated at room temperature for 15 min. Finally, the urea concentration in the sample was diluted to below 2 M, and trypsin (25200056, Thermo Fisher Scientific, USA) was added at a 1:50 (w/w) ratio, followed by overnight digestion at 37 °C. Subsequently, trypsin was added at a 1:100 (trypsin: protein) ratio, and digestion continued for 4 h.

After trypsin digestion, peptides were desalted using HyperSep™ C18 purification columns (60108-302, Thermo Fisher Scientific, USA) and dried under vacuum. The peptides were then reconstituted in 0.5 M TEAB (90114, Thermo Fisher Scientific, USA) and processed according to the manufacturer's instructions for the TMT labeling kit (90064CH, Thermo Fisher Scientific, USA). In brief, a unit of TMT reagent was thawed and reconstituted in acetonitrile (113212, Merck, USA). The peptide mixture was then incubated at room temperature for 2 h and desalted and dried using a vacuum centrifuge. Equal amounts of labeled peptides from each group were combined, and the dried peptides were resolubilized using Pierce™ High pH Reversed-Phase Peptide Fractionation Kit (84868, Thermo Fisher Scientific, USA). Finally, the samples were collected and combined into 15 fractions, and the dried peptides from each fraction were resuspended in 0.1% formic acid (159002, Merck, USA).

For nano-LC separation, 2 μg of peptides from each sample were loaded onto an Easy nLC 1200 nano-ultra performance liquid chromatography system (Thermo Fisher Scientific, USA). The samples were first loaded onto a Trap C18 column (100 μm × 20 mm, 5 μm) and then separated on a C18 analytical column (75 μm × 150 mm, 3 μm) using a gradient elution method at a flow rate of 300 nL/min. The mobile phase A was 0.1% formic acid in water, while the mobile phase B was 0.1% formic acid in water-acetonitrile solution (containing 95% acetonitrile). The gradient elution program was set as follows: 0 → 2 min, 2% → 8% B; 2 → 71 min, 8% → 28% B; 71 → 79 min, 28% → 40% B; 79 → 81 min, 40% → 100% B; 81 → 90 min, 100% B. The separated peptides were then subjected to mass spectrometry analysis using a Q-Exactive HFX mass spectrometer (Thermo Fisher Scientific, USA). The analysis duration was 60 min, the electrospray voltage was set at 2.1 kV, and the detection mode was positive ionization. The mass range for the precursor ion scan was 350–1200 m/z with a primary mass resolution of 60000@m/z 200, an AGC target of 3e6, and a primary maximum IT of 30 ms. The secondary mass resolution was set at 15000@m/z 200, with an AGC target of 1e6, a secondary maximum IT of 25 ms, HCD as the MS2 activation type, an isolation window of 20 Th, and a normalized collision energy of 32[98,99].

Database retrieval and data processing

LC-MS/MS data was processed using MaxQuant software (v.1.5.2.8), which included peptide identification and protein quantification. Tandem mass spectrometry searches were performed using the UniProt 14.1 (2009) - Gossypium hirsutum database and a decoy database. Trypsin/P was designated as the cleavage enzyme, allowing up to 2 missed cleavages. The initial search used a mass tolerance of 20 ppm, while the main search used a mass tolerance of 5 ppm, and the fragment ion mass tolerance was set at 0.02 Da. Filtering criteria included a peptide false discovery rate (FDR) threshold of ≤0.01, a protein FDR of ≤0.01, and peptide score distribution. Differential expression proteins (DEPs) between the LNP_T24 group and the si-PGC-1α LNP_T24 samples were selected using the "*T* test" in the R software, with a *P*-value < 0.05 as the threshold[98,100].

Protein-Protein Interaction (PPI) network

The DEPs were imported into the STRING database (https://cn.string-db.org/) for protein interaction network analysis and subcellular localization analysis. The Cytoscape software (version 3.9.0) was used to visualize the interaction network of proteins localized to mitochondria[101]. A schematic of the experimental workflow for the proteomics experiment can be found in Fig. S4 of the appendix. This figure provides a visual overview of the proteomics experiment, illustrating the various steps and processes involved.

Separation of nucleus and cytoplasm

The T24 cell line (LNP group and si-PGC-1α LNP group) was cultured in a 6-well plate. Cells in the 6-well plate were washed with 1×PBS (prepared using DEPC water) and centrifuged at 400 × *g* for 5 min. The cell pellet was quickly resuspended in a hypotonic lysis buffer (containing 10 mM HEPES (H109408-5g, Aladdin, Shanghai, China), pH 7.9, 1.5 mM MgCl2 (M434105-100g, Aladdin, Shanghai, China), 10 mM KCl (P433501-250g, Aladdin, Shanghai, China), 0.5 mM DTT (D301909-1ml, Aladdin, Shanghai, China), and washed with it. Then, the cells were lysed on ice for 10 min in the hypotonic lysis buffer containing 0.16 U/μL RNase inhibitor (R292575-1ml, Aladdin, Shanghai, China) and protease inhibitor (P301902-1 ml, Aladdin, Shanghai, China).

All lysates underwent differential centrifugation at 4 °C for 1500 × *g* (3 min), 3500 × *g* (8 min), and 17,000 × *g* (1 min), with the supernatant transferred to new centrifuge tubes after each spin. The nuclear pellet was washed 4 times with the hypotonic lysis buffer after centrifugation at 1500 × *g* for 3 min and then lysed in Reporter lysis buffer (E3971, Promega, USA), followed by incubation on ice for 10 min with a 21 G needle (60016589, KND, Shanghai, China), and finally centrifuged at 17,000 × *g* for 5 min at 4 °C.

The total lysate was collected from 3 wells of a 6-well plate containing Reporter lysis buffer, 16 U/μL RNase inhibitor, and protease inhibitor. Before centrifugation, it was lysed on ice for 10 min with a 21 G needle and then centrifuged at 17,000 × *g* for 5 min at 4 °C. The total and separated extracts were subjected to RNA extraction using Trizol reagent (15596026, Thermo Fisher Scientific, USA)[59].

RT-qPCR

The total RNA of the T24 cell line was extracted using Trizol reagent (15596026, Thermo Fisher Scientific, USA), and the concentration and purity of RNA were measured using a Nanodrop 2000 spectrophotometer. The RNA was reverse transcribed into cDNA using the PrimeScript RT reagent Kit (RR047A, Takara, Japan) according to the manufacturer's instructions. The reverse transcription conditions were 42 °C for 30–50 min, followed by 85 °C for 5 s.

For qRT-PCR detection, the Fast SYBR Green PCR Kit (RR820A, Takara, Japan) and the ABI PRISM 7300 RT-PCR system (Applied Biosystems) were used. The reaction conditions consisted of an initial denaturation step at 95 °C for 5 min, followed by 40 cycles of denaturation at 95 °C for 30 s, annealing at 57 °C for 30 s, and extension at 72 °C for 30 s. Three replicates were set up for each sample.

The relative expression levels of the genes were analyzed using the $2^{-\Delta\Delta Ct}$ method, where ΔΔCt = (average Ct value of the target gene in the experimental group - average Ct value of the reference gene in the experimental group) - (average Ct value of the target gene in the control group - average Ct value of the reference gene in the control group)[59,102]. The experiment was repeated three times. The primer sequences for RT-qPCR are shown in Table S3, and human β-Actin was used as the internal reference. The primers for β-Actin were synthesized by Wuxi AoRui Dongyuan Company (HP204660, OriGene Technologies, Wuxi, China).

FISH using Poly-dT

The T24 cell line was cultured under standard conditions until reaching the desired density. The cells were then divided into two groups for further treatment: one group served as the control and was treated with Lipofectamine LNP, while the other group was targeted for PGC-1α interference using siRNA lipid complex (si-PGC-1α LNP). Subsequently, the cells were fixed with 4% paraformaldehyde and permeabilized with PBS containing 0.1% Triton X-100 (BL934B, Baisha, Anhui, China) to facilitate the introduction and hybridization of Cy3-labeled oligo-adenosine (dT) probe (26-4320-02, Genelink, USA), which specifically binds to the Poly-A tail of mRNA.

The cell nuclei were stained with Hoechst dye (H412416-5mg, Aladdin, Shanghai, China), and images capturing the distribution of cell nuclei and Poly-A + RNA were acquired using fluorescence microscopy. Subsequently, Image J software was employed for quantitative analysis of the fluorescence signals to evaluate and compare the differences in the distribution of Poly-A + RNA between the nucleus and cytoplasm under the two treatment conditions[59].

RIP experiment

The T24 cell line (LNP group and si-PGC-1α LNP group) was selected for the RIP experiment. After the cells reached appropriate density, they were treated under UV conditions or formaldehyde cross-linking conditions. For UV cross-linking, the cells were treated with a UV-C irradiation of 0.3 J/cm² on ice, and the medium used was DEPC-treated PBS (B600154-0005, Bioscience, Zhejiang, China). As for formaldehyde cross-linking, the cells were treated with 1% formaldehyde (P1111, Solarbio, Beijing, China) for 10 minutes in a live state, followed by a 5-minute reaction termination at room temperature with 250 mM glycine (G8200, Solarbio, Beijing, China).

After cross-linking treatment, the cells were washed with DEPC-treated PBS and collected in ice-cold, RNase-free IP150 lysis buffer (prepared using DEPC-treated water, consisting of 50 mM HEPES pH 7.5, 150 mM NaCl, 10% glycerol (G8190, Solarbio, Beijing, China), 0.5% Triton X-100 (T8200, Solarbio, Beijing, China), 1 mM EDTA, 1 mM DTT, 1 μl RNase inhibitor, and protease inhibitor).

The cells were subjected to freeze-thaw cycles for 10 min with a 21 G needle, followed by a 10 min lysis on ice. Subsequently, the samples were centrifuged at 17000 × *g* for 5 min at 4 °C, and protein quantification was performed using the Bradford reagent. 5 mg (UV treatment) or 2 mg (formaldehyde treatment) of total protein was taken, and the concentration was adjusted to 1 mg/ml. The samples were incubated with pre-blocked goat anti-rabbit magnetic beads (D110555-0001, Bioscience, Zhejiang, China) containing 1% BSA and 5 μl/ml single-stranded DNA, along with 25 μL of the specific primary antibody anti-PGC-1α (rabbit; 1:1000, NBP1-04676, Novus Biologicals, USA). The incubation was carried out for 2 h (UV) or overnight (formaldehyde) at 4 °C with continuous rotation.

The washed beads were subsequently eluted with RNase-free lysis buffer for 30 min at 4 °C with rotation. For samples cross-linked with formaldehyde, the reverse cross-linking was achieved by heating at 70 °C for 1 h. Finally, RNA extraction was performed using PureZOL™ (7326880, Bio-Rad, USA) according to the manufacturer's protocol. The extracted RNA was re-suspended in 25 μl (input samples) or 15 μl (elution samples) of RNase-free water for subsequent analysis[59].

Co-IP experiment

T24 cells expressing Flag and 13myc tagged proteins, as well as PGC-1α::Flag and NXF1::13myc fusion proteins, were collected. The cells were lysed using NP-40 Lysis Buffer (P0013F, Beyotime, Shanghai, China) with the addition of Protease Inhibitor Cocktail (P1005, Beyotime, Shanghai, China) to prevent proteinase activity.

Next, the protein samples were divided into three portions. One portion was mixed with Anti-Flag magnetic beads (P2181S, Beyotime, Shanghai, China) and gently shaken to ensure the specific binding of Flag-tagged proteins. Another portion was mixed with Anti-Myc magnetic beads (P2183S, Beyotime, Shanghai, China) to ensure specific binding of MYC-tagged proteins. The remaining portion was saved for backup.

For further purification, the magnetic beads were washed with TBS buffer to remove nonspecifically bound proteins. Then, the Acid Elution Buffer provided in the magnetic bead kit was used to elute specifically bound proteins from the beads, followed by immediate neutralization using a Neutralization Buffer. Lastly, the eluted proteins were mixed with SDS-PAGE Sample Loading Buffer, separated using SDS-PAGE electrophoresis, and subjected to Western blotting for PPI analysis[59].

In vivo fluorescence experiment

The bladder cancer model was established through the following steps: firstly, T24 cells were formed into a monolayer and digested into single-cell suspension using trypsin. Then, the cell density was adjusted to 4×10^7 and suspended in 100 μl of PBS. Subsequently, the cell suspension was injected subcutaneously into the right armpit of each mouse. Once the T24 cells formed tumors (approximately 100 mm^3 in volume), the administration of complexes began.

The experiment employed female BALB/c nude mice (female, 8 weeks old, average weight of 24 ± 3 grams, purchased from Weitonglihua, Beijing, China) randomly divided into four groups with three nude mice each. All animals were housed under identical environmental conditions, including temperature, humidity, light/dark cycle, and feeding schedule. The nude mice were injected with 400 μl of si-PGC-1α LNP via the tail vein or subcutaneously in the back, as well as an equal amount of LNP, only si-PGC-1α, or PBS.

After administering the complexes, the nude mice were placed on a preheated platform inside a light-tight box. The nude mice were maintained under 2.5% isoflurane anesthesia. Images were captured using the Xenogen IVIS Lumina system (Caliper Life Sciences, USA) and analyzed with Living Image 3.1 software.

To evaluate the distribution of the complexes in vivo, the nude mice were euthanized 6 h after tail vein injection. The heart, lungs, liver, kidneys, spleen, and tumor tissue were collected and analyzed using the Xenogen IVIS Lumina system and Living Image 3.1 software.

In vivo antitumor activity in an orthotopic bladder cancer model

T24 cells (1×10^6 cells in 100 μL PBS) were subcutaneously injected into the bladders of female BALB/c nude mice (female, 8 weeks old, average body weight of 24 ± 3 grams, purchased from Weitonglihua, Beijing, China). After 14 days of tumor formation, the nude mice bearing tumors were randomly divided into four groups and intravesically treated with 500 μL si-PGC-1α LNP, equimolar dose of LNP, si-PGC-1α alone, or PBS solution. To prevent spontaneous urination, the animals were kept anesthetized for approximately 45 min. The treatment was repeated weekly for a duration of 5 weeks. Two days after the completion of the treatment, euthanasia was performed on the animals. Bladders were extracted, weighed, fixed in 4% PFA for 24 h, and then embedded in paraffin for histopathological analysis. Transverse sections were obtained from the middle of the bladders and stained with H&E.

In vivo anti-tumor activity in a lung metastasis model

T24 cells (5×10^6 cells, 100 μL PBS) were injected via the tail vein into 6-week-old female BALB/c nude mice (401, Viton Lihua, Beijing, China). After 50 days, a lung metastasis model of bladder cancer was successfully established. In this experiment, the nude mice with bladder cancer lung metastasis were randomly divided into four groups ($n = 6$ per group). The four groups of nude mice then received different treatments: one group received si-PGC-1α LNP, another received an equal dose of LNP, and the third and fourth groups received si-PGC-1α alone or PBS solution. The treatment was administered every 7 days for a total of 5 times. After completing the treatment, the nude mice were euthanized 48 h later. The lungs of the nude mice were then excised, photographed, and histologically examined. The number of visible metastatic nodules in each lung tissue was carefully counted[32,103].

Statistics and reproducibility

Statistical analysis was performed using R software v3.6.0 (R Foundation for Statistical Computing, Vienna, Austria) and SPSS software (version 21.0, IBM, USA). Descriptive data is presented as mean ± standard deviation. A non-paired t-test was used for comparisons between two groups, while a one-way analysis of variance (ANOVA) was applied for comparisons among multiple groups. Data visualization was conducted using GraphPad Prism version 9. A significance level of $P < 0.05$ was considered statistically significant. All experiments were conducted with appropriate sample sizes and replicates, with details specified in the Methods section. All experiments were reproducible and repeated at least three times to ensure reliability.

Reporting summary

Further information on research design is available in the Nature Portfolio Reporting Summary linked to this article.

Data availability

Proteomic data has been uploaded to a public database: iproX id IPX0011450000, ProteomeXchange id PXD062153. The access connection of data in ProteomeXchange is: http://proteomecentral.proteomexchange.org/cgi/GetDataset?ID=PXD062153. The access link for data in iProX is: https://www.iprox.cn/page/project.html?id=IPX0011450000. Metabolomics data has been uploaded to the public database iproX id IPX0011452000, ProteomeXchange id PXD062155. The access connection of data in ProteomeXchange is: http://proteomecentral.proteomexchange.org/cgi/GetDataset?ID=PXD062155. The access link for data in iProX is: https://www.iprox.cn/page/project.html?id=IPX0011452000. Sequencing data have been uploaded to the NCBI database under the BioProject accession number PRJNA1171889. The individual Sequence Read Archive (SRA) accession numbers are as follows: Disease group: SRR32814049, SRR32814048, SRR32814047; Control group: SRR32814052, SRR32814051, SRR32814050. All the numerical source data can be found at the Supplementary Data.

Received: 5 August 2024; Accepted: 6 May 2025;
Published online: 23 May 2025

References

1. Hensley, P. J. et al. Competing mortality risk from second primary malignancy in bladder cancer patients following radical cystectomy: Implications for survivorship. *Elsevier BV* **41**, 108.e11–108.e17 (2023).
2. Dyrskjøt, L. et al. Bladder cancer. *Springe. Sci. Bus. Media LLC* **9**, 58 (2023).
3. Martinez Rodriguez, R. H., Buisan Rueda, O. & Ibarz, L. Tumor vesical: presente y futuro. *Elsevier BV* **149**, 449–455 (2017).
4. Dobruch, J. & Oszczudłowski, M. Bladder Cancer: Current Challenges and Future Directions. *MDPI AG* **57**, 749 (2021).
5. Bouchelouche K. PET/CT in Bladder Cancer: An Update, Elsevier BV, (2022).
6. Lee, Y.-C. et al. The dynamic roles of the bladder tumour microenvironment. *Springe. Sci. Bus. Media LLC* **19**, 515–533 (2022).
7. Mori K., et al. Systemic therapies for metastatic hormone-sensitive prostate cancer: network meta-analysis, Wiley, (2021).
8. Katsila, T., Liontos, M., Patrinos, G. P., Bamias, A. & Kardamakis, D. The New Age of -omics in Urothelial Cancer – Re-wording Its Diagnosis and Treatment. *Elsevier BV* **28**, 43–50 (2018).
9. Alonso J. C. C. et al. OncoTherad® (MRB-CFI-1) Nanoimmunotherapy: A Promising Strategy to Treat Bacillus Calmette–Guérin-Unresponsive Non-Muscle-Invasive Bladder Cancer: Crosstalk among T-Cell CX3CR1, Immune Checkpoints, and the Toll-Like Receptor 4 Signaling Pathway, MDPI AG, (2023).
10. De Leo V., Maurelli A. M., Giotta L. & Catucci L. Liposomes containing nanoparticles: preparation and applications, Elsevier BV, (2022).
11. Yetisgin, A. A., Cetinel, S., Zuvin, M., Kosar, A. & Kutlu, O. Therapeutic Nanoparticles and Their Targeted Delivery Applications. *MDPI AG* **25**, 2193 (2020).
12. De Leo V., Milano F., Agostiano A. & Catucci L. Recent Advancements in Polymer/Liposome Assembly for Drug Delivery: From Surface Modifications to Hybrid Vesicles, MDPI AG, (2021).
13. Wang, et al. CaCO3/CaIP6 composite nanoparticles effectively deliver AKT1 small interfering RNA to inhibit human breast cancer growth, Informa UK Limited, (2015),
14. Montori-Grau, M. et al. Endoplasmic reticulum stress downregulates PGC-1α in skeletal muscle through ATF4 and an mTOR-mediated reduction of CRTC2. *Springe. Sci. Bus. Media LLC* **20**, 53 (2022).
15. Sannigrahi M. K. et al. HPV E6 regulates therapy responses in oropharyngeal cancer by repressing the PGC-1α/ERRα axis, American Society for Clinical Investigation, (2022)
16. Liu, S. et al. Role of irisin in physiology and pathology, Frontiers Media SA, (2022)
17. Popov L. Mitochondrial biogenesis: An update, Wiley, (2020).
18. Hayes, J. D., Dinkova-Kostova, A. T. & Tew, K. D. Oxidative Stress in Cancer. *Elsevier BV* **38**, 167–197 (2020).
19. Wu, Z. et al. Mechanisms Controlling Mitochondrial Biogenesis and Respiration through the Thermogenic Coactivator PGC-1. *Elsevier BV* **98**, 115–124 (1999).
20. LeBleu, V. S. et al. PGC-1α mediates mitochondrial biogenesis and oxidative phosphorylation in cancer cells to promote metastasis. *Springe. Sci. Bus. Media LLC* **16**, 1125 (2014).
21. Girnun, G. D. The diverse role of the PPARγ coactivator 1 family of transcriptional coactivators in cancer. *Elsevier BV* **23**, 381–388 (2012).
22. Pérez-Schindler J., et al. RNA-bound PGC-1α controls gene expression in liquid-like nuclear condensates, Proceedings of the National Academy of Sciences, (2021), 118.
23. Monsalve, M. et al. Direct Coupling of Transcription and mRNA Processing through the Thermogenic Coactivator PGC-1. *Elsevier BV* **6**, 307–316 (2000).
24. Chen, W., Yang, Q. & Roeder, R. G. Dynamic Interactions and Cooperative Functions of PGC-1α and MED1 in TRα-Mediated Activation of the Brown-Fat-Specific UCP-1 Gene. *Elsevier BV* **35**, 755–768 (2009).
25. Adamovich, Y. et al. The Protein Level of PGC-1α, a Key Metabolic Regulator, Is Controlled by NADH-NQO1. *Inf. UK Ltd.* **33**, 2603–2613 (2013).
26. Cho, H. et al. Transcriptional coactivator PGC-1α contains a novel CBP80-binding motif that orchestrates efficient target gene expression. *Cold Spring Harb. Lab.* **32**, 555–567 (2018).
27. Huang, Y., Yario, T. A. & Steitz, J. A. A molecular link between SR protein dephosphorylation and mRNA export. *Proc. Natl Acad. Sci.* **101**, 9666–9670 (2004).
28. Tavares, C. D. J. et al. Transcriptome-wide analysis of PGC-1α–binding RNAs identifies genes linked to glucagon metabolic action. *Proc. Natl Acad. Sci.* **117**, 22204–22213 (2020).
29. Bhalla, K. et al. PGC1α Promotes Tumor Growth by Inducing Gene Expression Programs Supporting Lipogenesis, American Association for. *Cancer Res. (AACR)* **71**, 6888–6898 (2011).
30. Krantz, S. et al. Mitophagy mediates metabolic reprogramming of induced pluripotent stem cells undergoing endothelial differentiation. *Elsevier BV* **297**, 101410 (2021).
31. Murata, Y., Jo, J. & Tabata, Y. Molecular Beacon Imaging System to Discriminate the Differentiation State of Cells from Energy Metabolic Pathways. *Am. Chem. Soc. (ACS* **8**, 2207–2218 (2023).

32. Liu, J. et al. Delivery of RIPK4 small interfering RNA for bladder cancer therapy using natural halloysite nanotubes, American Association for the Advancement of Science (AAAS), (2019).
33. NIU, X.-Y., PENG, Z.-L., DUAN, W.-Q., WANG, H. & WANG, P. Inhibition of HPV 16 E6 oncogene expression by RNA interference in vitro and in vivo. *Elsevier BV* **16**, 743–751 (2006).
34. Zhou, Q. et al. PGC-1α promotes mitochondrial respiration and biogenesis during the differentiation of hiPSCs into cardiomyocytes. *Elsevier BV* **8**, 891–906 (2021).
35. Compérat, E. et al. Current best practice for bladder cancer: a narrative review of diagnostics and treatments, Elsevier BV, (2022).
36. Cormio, A. et al. Mitochondrial dysfunctions in bladder cancer: Exploring their role as disease markers and potential therapeutic targets, Elsevier BV, (2017).
37. Díaz-Valdivia, N. et al. Mitochondrial Dysfunction and the Glycolytic Switch Induced by Caveolin-1 Phosphorylation Promote Cancer Cell Migration, Invasion, and Metastasis. *MDPI AG* **14**, 2862 (2022).
38. Huang, L. et al. LASS2 regulates invasion and chemoresistance via ERK/Drp1 modulated mitochondrial dynamics in bladder cancer cells. *Ivyspring Int. Publisher* **9**, 1017–1024 (2018).
39. Woolbright, B. L., Ayres, M. & Taylor, J. A. Metabolic changes in bladder cancer. *Elsevier BV* **36**, 327–337 (2018).
40. Andrzejewski, S. et al. PGC-1α Promotes Breast Cancer Metastasis and Confers Bioenergetic Flexibility against Metabolic Drugs. *Elsevier BV* **26**, 778–787.e5 (2017).
41. Tan, Z. et al. The Role of PGC1α in Cancer Metabolism and its Therapeutic Implications. *Am. Assoc. Cancer Res. (AACR* **15**, 774–782 (2016).
42. Zuo, Q. et al. PPARγ Coactivator-1α Suppresses Metastasis of Hepatocellular Carcinoma by Inhibiting Warburg Effect by PPARγ–Dependent WNT/β-Catenin/Pyruvate Dehydrogenase Kinase Isozyme 1 Axis. *Ovid Technol. (Wolters Kluwer Health* **73**, 644–660 (2021).
43. Gelato, K. A. et al. Super-enhancers define a proliferative PGC-1α-expressing melanoma subgroup sensitive to BET inhibition, Springer Science and Business Media LLC, (2017).
44. Vazquez, F. et al. PGC1α Expression Defines a Subset of Human Melanoma Tumors with Increased Mitochondrial Capacity and Resistance to Oxidative Stress. *Elsevier BV* **23**, 287–301 (2013).
45. Luo, C. et al. A PGC1α-mediated transcriptional axis suppresses melanoma metastasis. *Springe. Sci. Bus. Media LLC* **537**, 422–426 (2016).
46. Torrano, V.,et al. The metabolic co-regulator PGC1α suppresses prostate cancer metastasis, Springer Science and Business Media LLC, (2016).
47. Kaminski, L. et al. PGC1α Inhibits Polyamine Synthesis to Suppress Prostate Cancer Aggressiveness, American Association for. *Cancer Res. (AACR)* **79**, 3268–3280 (2019).
48. Valcarcel-Jimenez, L. et al. PGC1α Suppresses Prostate Cancer Cell Invasion through ERRα Transcriptional Control, American Association for. *Cancer Res. (AACR)* **79**, 6153–6165 (2019).
49. Yang S., et al. Multiomics integration reveals the effect of Orexin A on glioblastoma, Frontiers Media SA, (2023)
50. Mokhtari, K. et al. Colon cancer transcriptome. *Elsevier BV* **180-181**, 49–82 (2023).
51. Kochavi, A., Lovecchio, D., Faller, W. J. & Agami, R. Proteome diversification by mRNA translation in cancer. *Elsevier BV* **83**, 469–480 (2023).
52. Klebanoff C. A., Chandran S. S., Baker B. M., Quezada S. A. & Ribas A. T cell receptor therapeutics: immunological targeting of the intracellular cancer proteome, Springer Science and Business Media LLC, (2023).
53. Schmidt, D. R. et al. Metabolomics in cancer research and emerging applications in clinical oncology. *Wiley* **71**, 333–358 (2021).
54. Aghamiri S., Jafarpour A., Malekshahi Z. V., Mahmoudi Gomari M. & Negahdari B. Targeting siRNA in colorectal cancer therapy: Nanotechnology comes into view, Wiley, (2019).
55. Bahreyni, A. & Luo, H. Advances in Targeting Cancer-Associated Genes by Designed siRNA in Prostate Cancer. *MDPI AG* **12**, 3619 (2020).
56. Senapati, D. et al. Promising approaches of small interfering RNAs (siRNAs) mediated cancer gene therapy. *Elsevier BV* **719**, 144071 (2019).
57. Wei, R.-Q., Zhang, W.-M., Liang, Z., Piao, C. & Zhu, G. Identification of Signal Pathways and Hub Genes of Pulmonary Arterial Hypertension by Bioinformatic Analysis. *Wiley* **2022**, 1–12 (2022).
58. Dey N., Bhattacharjee S. Comparative transcriptomic data confirm the findings of dehydration stress-induced redox biology of indigenous aromatic rice cultivars, Springer Science and Business Media LLC, (2023).
59. Mihaylov, S. R. et al. The master energy homeostasis regulator PGC-1α exhibits an mRNA nuclear export function. *Springe. Sci. Bus. Media LLC* **14**, 5496 (2023).
60. Gouin, K. H. III et al. An N-Cadherin 2 expressing epithelial cell subpopulation predicts response to surgery, chemotherapy and immunotherapy in bladder cancer. *Springe. Sci. Bus. Media LLC* **12**, 4906 (2021).
61. Chen, X. et al. CD8+ T effector and immune checkpoint signatures predict prognosis and responsiveness to immunotherapy in bladder cancer. *Springe. Sci. Bus. Media LLC* **40**, 6223–6234 (2021).
62. Li Y., et al. An HGF-dependent positive feedback loop between bladder cancer cells and fibroblasts mediates lymphangiogenesis and lymphatic metastasis, Wiley, (2023).
63. Nam H., et al. The TGF-β/HDAC7 axis suppresses TCA cycle metabolism in renal cancer, American Society for Clinical Investigation, (2021)
64. Leo, M. et al. Transcriptomic Analysis of Colorectal Cancer Cells Treated with Oil Production Waste Products (OPWPs) Reveals Enrichment of Pathways of Mitochondrial Functionality. *MDPI AG* **11**, 3992 (2022).
65. Zhuang, L. et al. DYRK1B-STAT3 Drives Cardiac Hypertrophy and Heart Failure by Impairing Mitochondrial Bioenergetics. *Ovid Technol. (Wolters Kluwer Health* **145**, 829–846 (2022).
66. Jannig P. R., Dumesic P. A., Spiegelman B. M. & Ruas J. L. SnapShot: Regulation and biology of PGC-1α, Elsevier BV, (2022).
67. Chen, Q. M. Nrf2 for protection against oxidant generation and mitochondrial damage in cardiac injury. *Elsevier BV* **179**, 133–143 (2022).
68. Han, B. et al. Microglial PGC-1α protects against ischemic brain injury by suppressing neuroinflammation. *Springe. Sci. Bus. Media LLC* **13**, 47 (2021).
69. Halling, J. F. & Pilegaard, H. PGC-1α-mediated regulation of mitochondrial function and physiological implications. *Can. Sci. Publ.* **45**, 927–936 (2020).
70. Liu L., et al. Mitophagy receptor FUNDC1 is regulated by PGC-1α/NRF1 to fine tune mitochondrial homeostasis, Springer Science and Business Media LLC, (2021)
71. Anderson, R. M. et al. Dynamic regulation of PGC-1α localization and turnover implicates mitochondrial adaptation in calorie restriction and the stress response, Wiley, (2007).
72. Fernandez-Marcos, P. J. & Auwerx, J. Regulation of PGC-1α, a nodal regulator of mitochondrial biogenesis. *Elsevier BV* **93**, 884S–890S (2011).
73. Miller, K. N., Clark, J. P. & Anderson, R. M. Mitochondrial regulator PGC-1a—Modulating the modulator. *Elsevier BV* **5**, 37–44 (2019).
74. Puigserver, P. Tissue-specific regulation of metabolic pathways through the transcriptional coactivator PGC1-α. *Springe. Sci. Bus. Media LLC* **29**, S5–S9 (2005).

75. Scarpulla, R. C., Vega, R. B. & Kelly, D. P. Transcriptional integration of mitochondrial biogenesis. *Elsevier BV* **23**, 459–466 (2012).
76. Puigserver, P. et al. A Cold-Inducible Coactivator of Nuclear Receptors Linked to Adaptive Thermogenesis. *Elsevier BV* **92**, 829–839 (1998).
77. Lowell, B. B. & Spiegelman, B. M. Towards a molecular understanding of adaptive thermogenesis. *Springe. Sci. Bus. Media LLC* **404**, 652–660 (2000).
78. Cannon B., Nedergaard J. Brown Adipose Tissue: Function and Physiological Significance, American Physiological Society, (2004).
79. Lee, S. J. et al. Structural modification of siRNA for efficient gene silencing. *Elsevier BV* **31**, 491–503 (2013).
80. Jokisch, J.-F., Karl, A. & Stief, C. Intravesical immunotherapy in nonmuscle invasive bladder cancer. *Medknow* **31**, 304 (2015).
81. Larsen E. S., Joensen U. N., Poulsen A. M., Goletti D. & Johansen I. S. Bacillus Calmette–Guérin immunotherapy for bladder cancer: a review of immunological aspects, clinical effects and BCG infections, Wiley, (2020).
82. Maciejewski E. C., Basso M. A., Miller C. T. & Bailey M. R. The ethics of animal research and testing: A US perspective, Elsevier BV, (2023).
83. Kang M. R., et al. Intravesical Delivery of Small Activating RNA Formulated into Lipid Nanoparticles Inhibits Orthotopic Bladder Tumor Growth, American Association for Cancer Research (AACR), (2012).
84. Arunachalam, D. et al. Expression of immune response genes in human corneal epithelial cells interacting with Aspergillus flavus conidia. *Springe. Sci. Bus. Media LLC* **23**, 5 (2022).
85. Linkner, T. R. et al. Cellular Proteo-Transcriptomic Changes in the Immediate Early-Phase of Lentiviral Transduction. *MDPI AG* **9**, 2207 (2021).
86. Deng, Y.-J. et al. GRB10 and E2F3 as Diagnostic Markers of Osteoarthritis and Their Correlation with Immune Infiltration. *MDPI AG* **10**, 171 (2020).
87. Peng, X. Y., Wang, Y., Hu, H., Zhang, X. J. & Li, Q. Identification of the molecular subgroups in coronary artery disease by gene expression profiles. *Wiley* **234**, 16540–16548 (2019).
88. Panigrahi, B., Singh, R. K., Mishra, S. & Mandal, D. Cyclic peptide-based nanostructures as efficient siRNA carriers. *Inf. UK Ltd.* **46**, 763–773 (2018).
89. Wang, W. et al. The Role of TKS5 in Chromosome Stability and Bladder Cancer Progression. *MDPI AG* **23**, 14283 (2022).
90. Eun, J. W. et al. Cancer-associated fibroblast-derived secreted phosphoprotein 1 contributes to resistance of hepatocellular carcinoma to sorafenib and lenvatinib. *Wiley* **43**, 455–479 (2023).
91. Salem, M., Shan, Y., Bernaudo, S. & Peng, C. miR-590-3p Targets Cyclin G2 and FOXO3 to Promote Ovarian Cancer Cell Proliferation, Invasion, and Spheroid Formation. *MDPI AG* **20**, 1810 (2019).
92. Shu, M. et al. Targeting oncogenic miR-335 inhibits growth and invasion of malignant astrocytoma cells. *Springe. Sci. Bus. Media LLC* **10**, 59 (2011).
93. Chi, N.-F. et al. Untargeted metabolomics predicts the functional outcome of ischemic stroke. *Elsevier BV* **120**, 234–241 (2021).
94. Yu, M. et al. Molecular classification and clinical diagnosis of acute-on-chronic liver failure patients by serum metabolomics. *Elsevier BV* **198**, 114004 (2021).
95. Ye, X. et al. A urine and serum metabolomics study of gastroesophageal reflux disease in TCM syndrome differentiation using UPLC-Q-TOF/MS. *Elsevier BV* **206**, 114369 (2021).
96. Chen, L. et al. TIM-1 promotes proliferation and metastasis, and inhibits apoptosis, in cervical cancer through the PI3K/AKT/p53 pathway, Springer Science and Business Media LLC, (2022).
97. Branco A., Bartley S. M., King S. N., Jetté M. E. & Thibeault S. L. Vocal fold myofibroblast profile of scarring, Wiley, (2015).
98. Guo, H. et al. Dynamic TMT-Based Quantitative Proteomics Analysis of Critical Initiation Process of Totipotency during Cotton Somatic Embryogenesis Transdifferentiation. *MDPI AG* **20**, 1691 (2019).
99. Wang, Z. et al. Plasma proteome profiling of high-altitude polycythemia using TMT-based quantitative proteomics approach. *Elsevier BV* **194**, 60–69 (2019).
100. Friedrich, C. et al. Comprehensive micro-scaled proteome and phosphoproteome characterization of archived retrospective cancer repositories. *Springe. Sci. Bus. Media LLC* **12**, 3576 (2021).
101. Mahmoudi A., Atkin S. L., Nikiforov N. G. & Sahebkar A. Therapeutic Role of Curcumin in Diabetes: An Analysis Based on Bioinformatic Findings, MDPI AG, (2022).
102. Jin, D. et al. RETRACTED ARTICLE: m6A mRNA methylation initiated by METTL3 directly promotes YAP translation and increases YAP activity by regulating the MALAT1-miR-1914-3p-YAP axis to induce NSCLC drug resistance and metastasis, Springer Science and Business Media LLC, (2019).
103. Xie, B. et al. CircXRN2 suppresses tumor progression driven by histone lactylation through activating the Hippo pathway in human bladder cancer. *Springe. Sci. Bus. Media LLC* **22**, 151 (2023).

Acknowledgements

This study was supported by Liaoning Plan Project of Science and Technology (Grant No. 2022-MS-190). National Natural Science Foundation of China (Grand No. 82002669). Science and Technology Planning Project of Liaoning Province of China (2023JH2/20200090).

Author contributions

Zhenghua Liu, Peng Xin, and Weiwei Wu contributed equally to the experimental design and data collection. Mingyue Jin conducted metabolomic analyses and assisted with the interpretation of metabolic pathway disruptions. Yang Du provided support for in vivo experiments and animal model analysis. Hao Zhang, Tao Liu, and Yuanjun Jiang conceptualized the study, supervised the research, and provided critical insights into the manuscript preparation. Hao Zhang was primarily responsible for nanoparticle synthesis and siRNA delivery methodology. Tao Liu and Yuanjun Jiang directed the transcriptomic and proteomic analyses and contributed to the discussion of results. All authors contributed to manuscript drafting and approved the final version for submission.

Competing interests

The authors declare no competing of interests.

Ethical approval

All experimental procedures involving animals were approved by the Institutional Animal Care and Use Committee of the Department of Urology, Shengjing Hospital of China Medical University under approval number CMUXN2023039.

Additional information

Supplementary information The online version contains supplementary material available at https://doi.org/10.1038/s42003-025-08174-w.

Correspondence and requests for materials should be addressed to Yuanjun Jiang, Tao Liu or Hao Zhang.

Peer review information *Communications Biology* thanks Joo-In Park, Gloria Salazar, and the other, anonymous, reviewer for their contribution to the peer review of this work. Primary Handling Editors: Bibekanand Mallick and Kaliya Georgieva.